

RESEARCH ARTICLE SUMMARY

NEUROIMMUNOLOGY

Heterogeneity of meningeal B cells reveals a lymphopoietic niche at the CNS borders

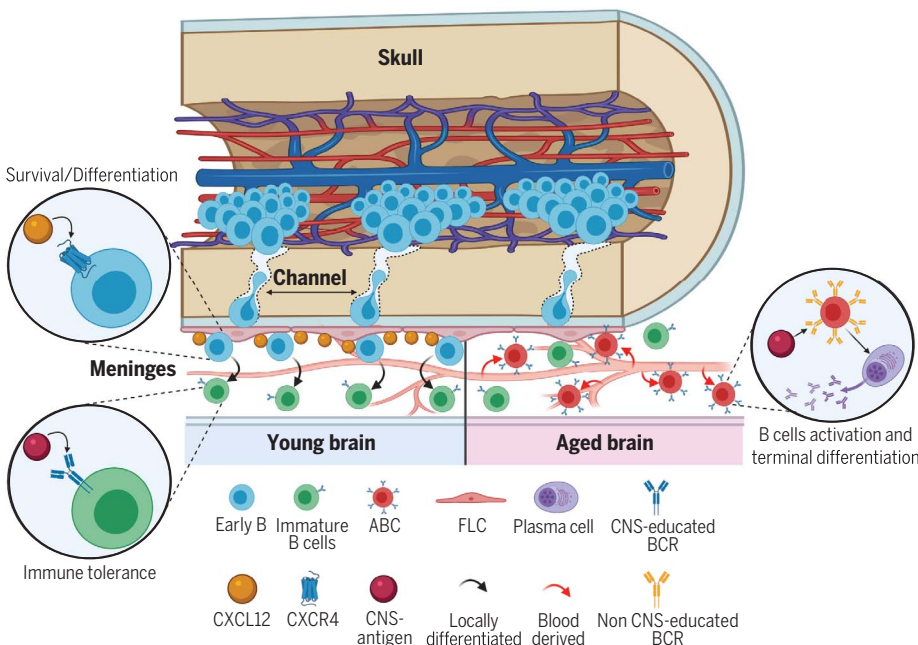
Simone Brioschi[†], Wei-Le Wang[†], Vincent Peng[†], Meng Wang, Irina Shchukina, Zev J. Greenberg, Jennifer K. Bando, Natalia Jaeger, Rafael S. Czepielewski, Amanda Swain, Denis A. Mogilenko, Wandy L. Beatty, Peter Bayguinov, James A. J. Fitzpatrick, Laura G. Schuettelpelz, Catrina C. Fronick, Igor Smirnov, Jonathan Kipnis, Virginia S. Shapiro, Gregory F. Wu, Susan Gilfillan, Marina Cella, Maxim N. Artyomov, Steven H. Kleinstein, Marco Colonna*

INTRODUCTION: The meninges are a three-layer membrane that covers the central nervous system (CNS): The outermost layer, the dura mater, is attached onto the skull periosteum; the two inner layers, the arachnoid and the pia mater, cover the brain cortex. The meningeal compartment hosts both innate and adaptive immune cells, providing constant immunosurveillance of the CNS border regions. Given its strategic location, meningeal immunity is a key component of neuroimmune disorders. Recent studies have investigated the origin and dynamics of meningeal myeloid cells. However, little is known about meningeal B cells.

RATIONALE: To investigate the phenotype of meningeal B cells, we used different high-

throughput techniques, such as single-cell RNA sequencing (scRNA-seq), cytometry by time of flight (CyTOF), and single-cell B cell receptor sequencing (scBCR-seq). We further corroborated our finding by flow cytometry and confocal imaging. We determined the origin of meningeal B cells by bone marrow transplantation (BMT) and parabiosis experiments. Lastly, we investigated how meningeal B cells change during aging.

RESULTS: We characterized the mouse meninges using scRNA-seq, which revealed that meningeal B cells encompass multiple stages of their development, spanning pro-B to mature B cells. Identical subsets were found in the bone marrow (BM), but not in the blood. CyTOF and flow



Composition of meningeal B cells in young and aged mice. Meningeal B cells originate from the calvaria and migrate to the meninges through skull vascular channels. These B cells complete their development locally, where fibroblast-like cells (FLCs) provide critical factors for survival and differentiation of early B cells (i.e., CXCL12). At this stage, CNS-antigen experience induces immune tolerance. In aged mice, age-associated B cells (ABCs) infiltrate the meninges from the periphery and differentiate into Ig-secreting plasma cells upon encounter with CNS antigens.

cytometry further confirmed this result, demonstrating that early B cell subsets that are normally present in the BM are also found in the meninges under homeostasis. BMT with selective reconstitution of the skull BM showed that meningeal B cells are derived from the calvaria; namely, the hematopoietic region located within the cranial flat bones. We then performed parabiosis between wild-type and CD19-Tomato mice, which express the tdTomato fluorescent protein specifically in B cells. This experiment demonstrated that circulating B cells minimally infiltrated the mouse meninges under homeostasis. Using confocal imaging, we showed that B cells migrate from the calvaria to the meninges through specialized vascular channels traversing the inner skull bone. Interactome analysis of our scRNA-seq data highlighted a network of molecular communications between meningeal B cells and dura fibroblast-like cells (FLCs). Notably, we showed that FLCs express high levels of *Cxcl12*, whereas dura early B cells express its receptor *Cxcr4*. Expression of these molecules in the respective populations was validated by imaging and flow cytometry. The CXCL12–CXCR4 axis is required for the survival and differentiation of early B cells in the BM, and the same mechanism may be present in the dura. We also showed that aged mice (~2 years of age) accumulate age-associated B cells (ABCs) and plasma cells in the dura. Compared to naïve B cells, ABCs featured important transcriptional changes, as well as reduced diversity of the V-region repertoire and accumulation of somatic mutations, thus indicating antigen experience. Analysis of B cells clones by scBCR-seq showed that dura ABCs infiltrated from the periphery. On the basis of BCR clonality, we also suggest that dura ABCs may locally undergo terminal differentiation into immunoglobulin (Ig)-secreting plasma cells.

CONCLUSION: This study reveals that mouse meninges harbor a lymphopoietic niche specific for the CNS borders. B cell development in the meninges may induce immune tolerance against CNS antigens, thus preserving immune privilege within the CNS. However, blood-derived ABCs accumulate in the meninges over time. Peripheral ABCs are not educated by the CNS antigens and may locally differentiate into CNS-reactive plasma cells. This condition may endanger the immune-privileged CNS environment during aging. ■

The list of author affiliations is available in the full article online.

*Corresponding author. Email: mcolonna@wustl.edu

[†]These authors contributed equally to this work.

Cite this article as S. Brioschi et al., *Science* 373, eabf9277 (2021). DOI: 10.1126/science.abf9277

READ THE FULL ARTICLE AT
<https://doi.org/10.1126/science.abf9277>

RESEARCH ARTICLE

NEUROIMMUNOLOGY

Heterogeneity of meningeal B cells reveals a lymphopoietic niche at the CNS borders

Simone Brioschi^{1†}, Wei-Le Wang^{1†}, Vincent Peng^{1†}, Meng Wang², Irina Shchukina¹, Zev J. Greenberg³, Jennifer K. Bando⁴, Natalia Jaeger¹, Rafael S. Czepielewski¹, Amanda Swain¹, Denis A. Mogilenko¹, Wandy L. Beatty⁵, Peter Bayguinov⁶, James A. J. Fitzpatrick^{6,7,8}, Laura G. Schuettelpelz³, Catrina C. Fronick⁹, Igor Smirnov¹, Jonathan Kipnis¹, Virginia S. Shapiro¹⁰, Gregory F. Wu¹¹, Susan Gilfillan¹, Marina Cella¹, Maxim N. Artyomov¹, Steven H. Kleinstein^{2,12}, Marco Colonna^{1*}

The meninges contain adaptive immune cells that provide immunosurveillance of the central nervous system (CNS). These cells are thought to derive from the systemic circulation. Through single-cell analyses, confocal imaging, bone marrow chimeras, and parabiosis experiments, we show that meningeal B cells derive locally from the calvaria, which harbors a bone marrow niche for hematopoiesis. B cells reach the meninges from the calvaria through specialized vascular connections. This calvarial-meningeal path of B cell development may provide the CNS with a constant supply of B cells educated by CNS antigens. Conversely, we show that a subset of antigen-experienced B cells that populate the meninges in aging mice are blood-borne. These results identify a private source for meningeal B cells, which may help maintain immune privilege within the CNS.

The central nervous system (CNS) is enveloped by the meninges, which harbor different immune cell types that provide constant surveillance at the CNS border (1–3). Although meningeal lymphocytes are thought to derive exclusively from the systemic circulation, recent findings question this premise. Vascular connections between the calvaria (the flat bones forming the top dome of the skull) and meninges have recently been described (4–6), and two multi-dimensional studies identified a cluster of developmentally immature B cells in the mouse CNS (7, 8). We hypothesized that these B cells may derive from calvarial hematopoiesis. Here, we show that meningeal B cells encompass

multiple stages of B cell development, spanning pro-B to mature B cells. Using parabiotic mice and bone marrow (BM) chimeras with selective reconstitution of the skull BM, we demonstrate that most meningeal B cells originate from the calvaria. We envision that calvaria-derived B cells are locally educated by CNS-derived antigens to prevent the generation of immunoglobulins (Igs) with high affinity for CNS epitopes. Conversely, a population of age-associated B cells (ABCs) infiltrates the mouse meninges from the circulation during aging. This study sheds light on the origin and phenotypes of meningeal B cells in homeostasis and during aging, challenging the widely accepted idea that meningeal adaptive immunity originates exclusively from systemic circulation.

Results

Meningeal B cells are extravascular and can exit the CNS compartment through the dura lymphatics

Meninges are formed by three membranes. The dura mater is the outermost layer attached onto the skull periosteum, whereas the two inner layers, the arachnoid and pia mater (leptomeninges), cover the brain cortex (Fig. 1A). This region is enriched in different immune cell types, and B cells represent about 30% of the total CD45⁺ cells in mouse meninges (Fig. 1B and fig. S1A). Because the dura contains a relative abundance of immune cells and can be more easily dissected than the leptomeninges, we focused most of our subsequent studies on dural B cells. By flow cytometry, B cells were found in samples of both the dura mater and the brain and leptomeninges (fig. S1B). The majority of meningeal B cells in young-adult

mice were B2 type, whereas innate B cells (B1a and B1b) represented a minor population (fig. S1C). We surveyed B cells by confocal imaging in the brain and spinal cord of *Cd19*^{Cre}; *Rosa26*^{tdTomato} mice (hereafter CD19-Tomato), which express the tdTomato fluorescent protein specifically in CD19⁺ cells (9). Although no B cells were found in the brain parenchyma (fig. S1D), B cells were present in the leptomeninges along the brain surface (fig. S1E), indicating that brain B cells are extravascular. Two-photon in vivo imaging in the subdural space of the CD19-Tomato mice showed that most meningeal B cells were localized in the extravascular compartment (Fig. 1, C and D) and appeared relatively immobile as compared to intravascular B cells (Fig. 1, E and movie S1). The dura mater contains blood and lymphatic vessels (LVs) along the sagittal and transverse sinuses (fig. S2A). These areas were particularly enriched in B cells, some of which were located within dura LVs (fig. S2B). Dura lymphatics drain immune cells and molecules to the cervical lymph nodes (cLNs) (10, 11), suggesting that meningeal B cells may undergo a similar fate. To test this hypothesis, we introduced CD19-Tomato splenocytes into the cerebrospinal fluid (CSF) of wild-type mice by intracisterna magna (ICM) injection (Fig. 1F), and 24 hours later CD19-Tomato B cells were found accumulating in the cLNs (Fig. 1, G and H). Donor-derived B cells appeared to be located in both the dura LVs and cLN B cell zone (Fig. 1, I and J). Thus, LVs may serve as a migratory route for B cells exiting the CNS compartment.

Meningeal B cells are phenotypically similar to bone marrow B cells

Although B cells represent a main immune population in the meninges, little is known about their composition under homeostasis. A previous single-cell RNA sequencing (scRNA-seq) study on mouse brain immune cells identified two distinct B cell subsets, labeled as “mature” and “immature” (7). We reclustered these transcriptomic data (GSE98969) and identified B cells based on the enrichment of Ig transcripts (Fig. 2A). This population uniformly expressed pan-B cell signature genes (*Cd79b* and *Cd19*). However, mature B cell genes (*H2-Aa* and *Ms4a1*) and early B cell genes (*Rag1* and *Cd93*) appeared unevenly distributed in this cluster (Fig. 2B), suggesting that B cells in the CNS encompass different stages of their development. Next, we compared the phenotype of meningeal B cells to that of B cells in the BM, blood, and spleen (Fig. 2C). Based on the Hardy fraction (12, 13), early B cells were identified as CD19⁺B220^{lo}CD43^{hi} (bona fide fraction B-C), late B cells as CD19⁺B220^{lo}CD43^{lo} (bona fide fraction D-E), and mature B cells as CD19⁺B220^{hi}CD43⁻ (fraction F). BM and meningeal B cells appeared

¹Department of Pathology and Immunology, Washington University School of Medicine, Saint Louis, MO 63110, USA. ²Interdepartmental Program in Computational Biology and Bioinformatics, Yale University, New Haven, CT 06511, USA. ³Department of Pediatrics, Washington University School of Medicine, Saint Louis, MO 63110, USA. ⁴Department of Microbiology and Immunology, Stanford University School of Medicine, Stanford, CA 94305, USA. ⁵Department of Molecular Microbiology, Center for Infectious Disease Research, Washington University School of Medicine, Saint Louis, MO 63110, USA. ⁶Washington University Center for Cellular Imaging, Washington University School of Medicine, Saint Louis, MO 63110, USA. ⁷Departments of Cell Biology and Physiology and Neuroscience, Washington University School of Medicine, Saint Louis, MO 63110, USA. ⁸Department of Biomedical Engineering, Washington University in Saint Louis, Saint Louis, MO 63130, USA. ⁹McDonnell Genome Institute, Washington University School of Medicine, Saint Louis, MO 63110, USA. ¹⁰Department of Immunology, Mayo Clinic, Rochester, MN 55905, USA. ¹¹Department of Neurology, Washington University in Saint Louis, Saint Louis, MO 63110, USA. ¹²Department of Pathology, Yale School of Medicine, New Haven, CT 06520, USA.

*Corresponding author. Email: mcolonna@wustl.edu

†These authors contributed equally to this work.

Fig. 1. B cells represent a major immune cell type in mouse meninges and are capable of trafficking through meningeal lymphatics.

(A) Cartoon representing the structural organization of the meninges. (B) Representative flow cytometry plot showing the proportion of B cells within the overall CD4⁺ population in mouse dura (average of $n = 4$ mice, data generated from a single experiment).

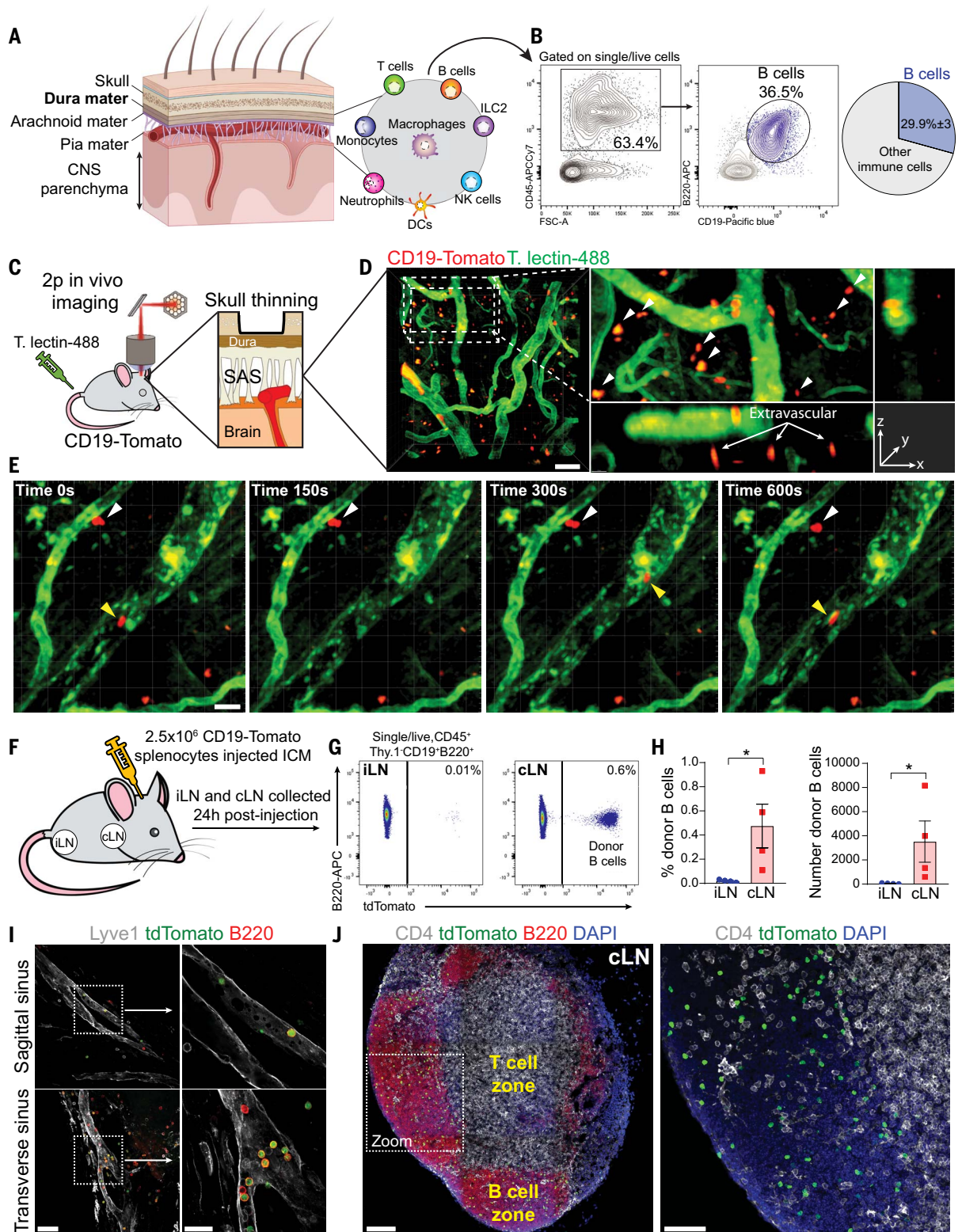
(C) Schematic depiction of the experimental approach to perform in vivo two-photon imaging in the subdural space of CD19-Tomato mice.

(D) Representative two-photon image of extravascular B cells in CD19-Tomato mouse meninges (scale bar: 50 μm). Images on the right are enlarged from box.

(E) Two-photon time-lapse imaging in the meninges of a CD19-Tomato mouse. Intra-vascular B cells: yellow arrowheads; extravascular B cells: white arrowheads (scale bar: 20 μm).

(F) Schematic

depiction of the experimental approach (ICM: intracisterna magna). (G) Flow cytometry analysis of donor (CD19-Tomato)-derived B cells in inguinal lymph nodes (iLNs) and cervical lymph nodes (cLNs) 24 hours after injection. (H) Frequency and absolute number of donor-derived B cells in iLNs and cLNs (mean \pm SEM; $n = 4$ mice; Mann-Whitney U test, * $P < 0.05$; data generated from a single experiment). (I) Confocal images of donor (CD19-



Tomato) B cells trafficking through the dura lymphatics 24 hours after injection (representative of $n = 4$ mice, data generated from a single experiment) [scale bars: 50 μm (left) and 20 μm (right)]. (J) Confocal image of donor (CD19-Tomato)-derived B cells in cLNs 24 hours after injection (representative of $n = 4$ mice, data generated from a single experiment) [scale bars: 100 μm (left) and 50 μm (right)].

Fig. 2. Mouse meninges harbor a heterogeneous B cell population that encompasses multiple developmental stages.

(A) Uniform manifold approximation and projection (UMAP) of CD45⁺ brain cells from a deposited scRNA-seq dataset (GSE98969). Normalized expression for *Ighm*, *Igkc*, and *Iglc2* was color coded for transcript counts. The cell cluster highly enriched for the gene set was inferred as B cells.

(B) Enrichment for transcripts linked to different B cell maturation stages. Pan-B cell: *Cd79b* and *Cd19*; mature B cell: *H2-Aa* and *Ms4a1*; and immature B cell: *Rag1* and *Cd93*.

(C) Flow cytometry analysis of B cells from the BM, brain, dura, blood, and spleens of C57BL/6 mice. B cells were gated as CD45⁺CD19⁺ and lineage (CD3, CD11b, F4/80, and Gr-1)-negative (left column) and were further divided into early (B220^{lo}CD43^{hi}), late (B220^{lo}CD43^{lo}), and mature (B220^{hi}CD43⁻) subset (middle column). CD93 and IgM staining is shown for the three subsets (right column).

(D) Flow cytometry analysis of *Rag1*^{-/-} mice. B cells derived from BM, brain, and dura were gated as CD19⁺ and lineage (CD3, CD11b, F4/80, and Gr-1)-negative (left column) and were further divided into early (B220^{lo}CD43^{hi}), late (B220^{lo}CD43^{lo}), and mature (B220^{hi}CD43⁻) subsets (right column).

(E) Quantification of B cell subsets in BM, brain and dura of C57BL/6 and *Rag1*^{-/-} mice (*n* = 8 and 7 mice, respectively; data generated from two independent experiments).

(F) Representative confocal images of the dura mater from *Rag1*^{GFP} mice (scale bar: 100 μm). (G) Representative confocal image of IgM⁺ (yellow arrowhead) and IgM⁻ B cells (red arrowhead) in CD19-Tomato mice [scale bars: 1 mm (left) and 50 μm (right)].

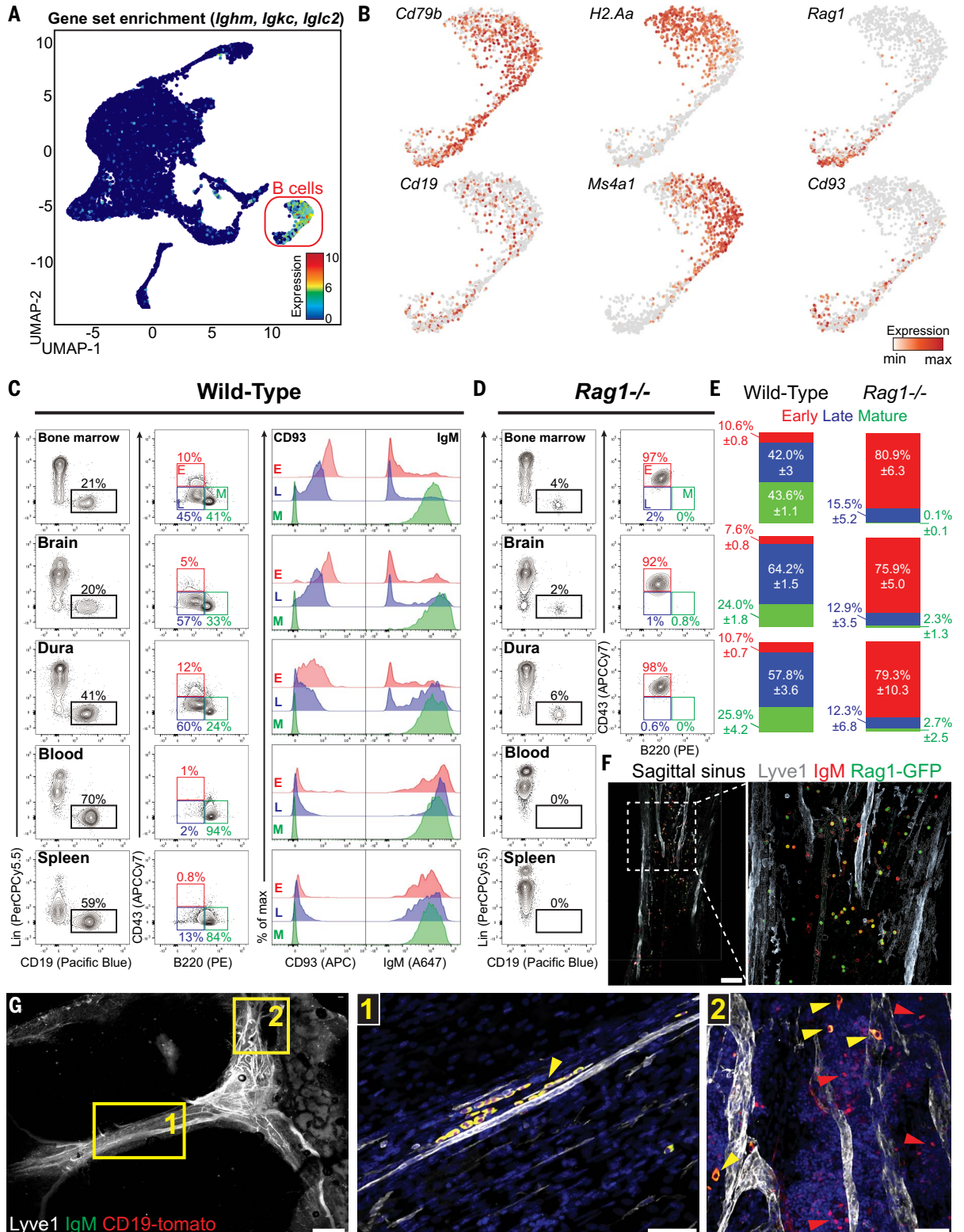
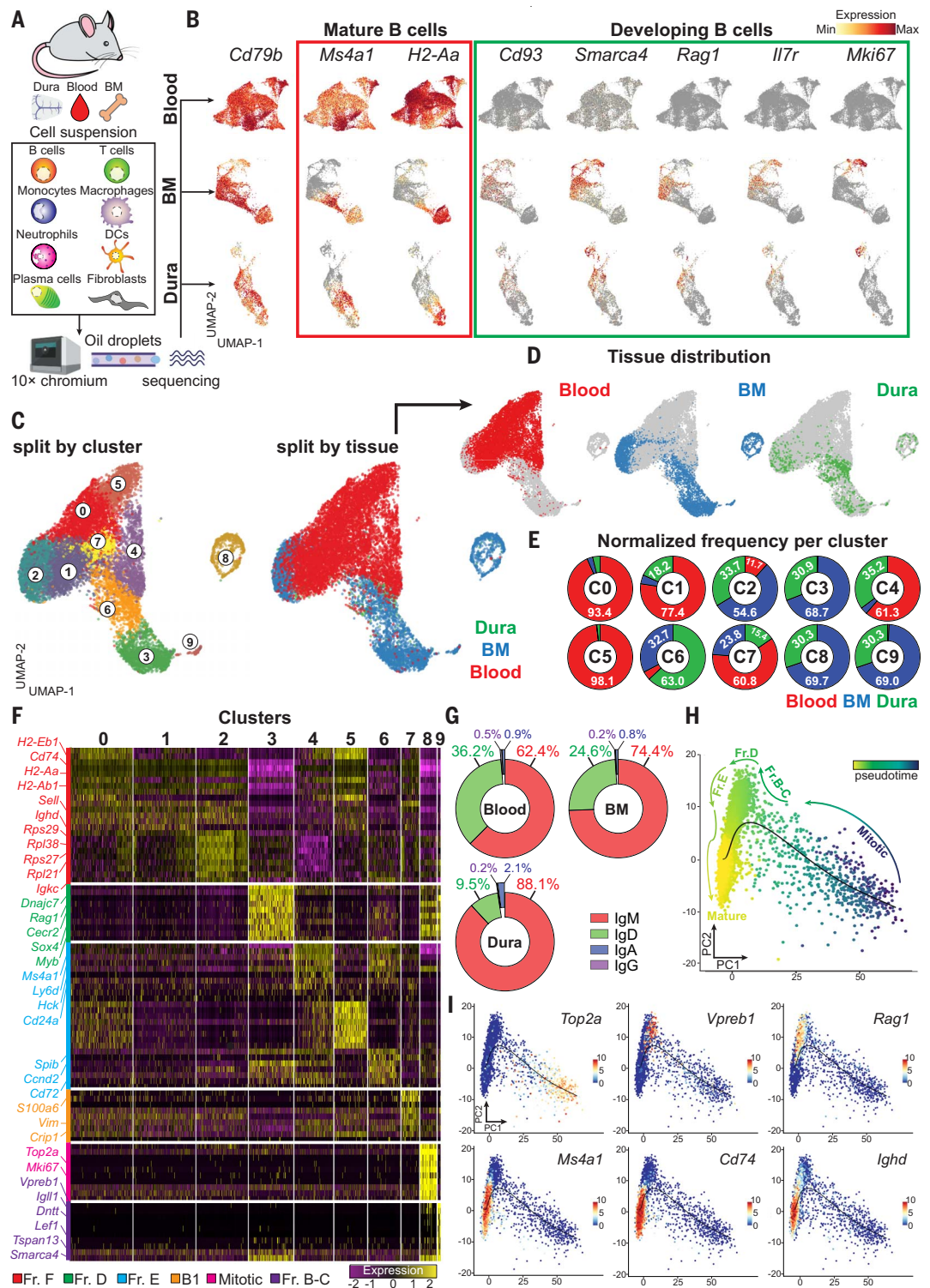


Fig. 3. scRNA-seq analysis reveals a similar transcriptomic pattern in dura and BM B cells.

(A) Schematic depiction of the experimental design related to scRNAseq. (B) Expression of featured genes denoting mature and developing B cells in blood, BM, and dura. (C) UMAP of 13,281 B cells aggregated from blood, BM, and dura collected from three C57BL6 mice and colored by cluster (left) or tissue origin (right) (data generated from a single experiment). (D) UMAP plots split by tissue showing the distribution of blood, BM, and dural B cells. (E) Proportional contribution of the three tissues (blood, BM, and dura) to these 10 B cell clusters. (F) Gene expression heatmap of the top 10 signature genes per cluster. (G) Frequency of C-region usage per tissue determined by scBCRseq. (H) Developmental trajectory displayed on PCA (principal component analysis) map and colored by slingshot pseudotime. (I) Enrichment of key transcripts differentially expressed throughout B cell maturation.



similarly distributed into these three subsets. In both compartments, early B cells were IgM⁺CD93⁺, mature B cells were IgM⁺CD93⁻, and late B cells had an intermediate phenotype. By contrast, most blood and spleen B cells exhibited a mature phenotype. We then repeated this analysis in *Rag1*^{-/-} mice, which lack mature B cells (Fig. 2D), and found a

population of B220^{lo}CD43^{hi} B cells in the BM, brain, and dura, whereas the blood and spleen completely lacked B cells. Thus, the composition of meningeal B cells closely resembles that of the BM, both in wild-type and *Rag1*^{-/-} mice (Fig. 2E). As a validation, we imaged the dura mater from *Rag1*^{GFP} knock-in mice (14) and found *Rag1*-expressing B cells,

preferentially located along the sagittal sinus (Fig. 2F and fig. S3A). We also performed confocal imaging of the dura mater from CD19-Tomato mice stained for immunoglobulin M (IgM) and found distinct subsets of IgM⁺ and IgM⁻ B cells (Fig. 2G). Immunofluorescent imaging of CD93, Ki67, GL7 (markers of early B cells), and CD20 (marker of mature B cells) in

Downloaded from https://www.science.org at Academia Sinica Life Science on November 30, 2022

Fig. 4. Mass cytometry confirms developmental heterogeneity of dura B cells.

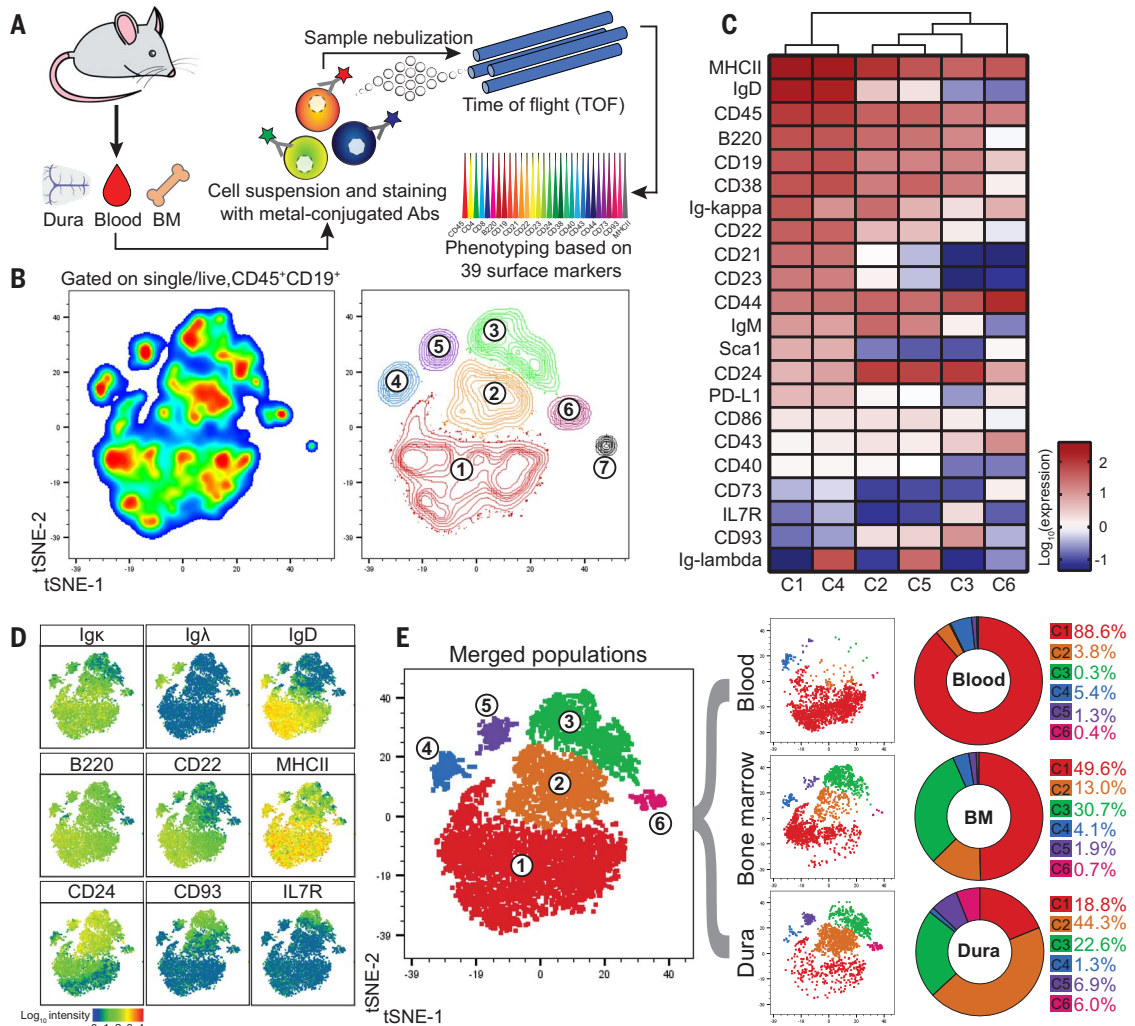
(A) Schematic depiction of the experimental design related to cytometry by time of flight (CyTOF) analysis.

(B) Unsupervised clustering by means of t-distributed stochastic neighbor embedding (t-SNE) of 6000 live singlet CD45⁺CD19⁺ B cells obtained from concatenation of three tissues (blood, BM, and dura) collected from three C57BL/6 mice (data generated from a single experiment). Cells are displayed by pseudo-color (left) and contour plots (right).

(C) Heatmap showing the surface protein expression of selected B cell markers among the six B cell clusters (cluster 7 was arbitrarily excluded because of low cell number).

(D) Staining enrichment of representative surface markers for mature and developing B cells.

(E) Merged t-SNE plot colored by cluster (left) and t-SNE plot split by tissue (middle). Frequency of each cluster in blood, BM, and dura (right).



the dura mater confirmed that early B cells are present in mouse meninges under homeostasis (fig. S3B). Lastly, we analyzed the expression of various markers differentially expressed across B cell development and confirmed that BM and meninges harbor overlapping B cell phenotypes (fig. S4).

Single-cell analyses resolve multiple developmental stages of dura B cells

To gain in-depth insight into the diversity of meningeal B cells, we performed scRNA-seq of cells isolated from dura mater, blood, and BM. We analyzed unsorted cell suspensions to minimize experimental artifacts due to cell stress and to include both immune and non-immune cells (Fig. 3A). Cells that passed the quality control underwent unsupervised clustering and were displayed on the Uniform Manifold Approximation and Projection (UMAP) space (figs. S5 to S7). In the dura mater, we resolved clusters of neutrophils (43.7%), B cells (26.3%), T cells (3.2% double negative, 2.8% CD8⁺, and 1.7% CD4⁺), monocytes (2.5% Ly6C⁺, 1.2% Ly6C⁻), natural killer cells (1.6%), macro-

phages (1.3%), mast cells (1.1%), plasmacytoid dendritic cells (pDCs) (1%), classical dendritic cells (cDCs) (0.9%), type 2 innate lymphoid cells (ILC2) (0.4%), and plasma cells (0.3%) (fig. S5). Dura fibroblasts (5.7%) were identified from the expression of *Coll1a* and *Mgp*, as recently reported (15). Focusing on the B cell compartment, we found multiple B cell clusters in all analyzed tissues. Indeed, all B cells in the blood exhibited a rather homogeneous expression of the mature markers *Ms4a1* and *H2-Aa*, whereas the early B cell markers *Cd93*, *Smarca4*, *Rag1*, *IL7r*, and *Mki67* were not detected (Fig. 3B). The diversity in blood B cells was mostly driven by the expression of κ or λ light chains (fig. S7). By contrast, B cells in the BM and dura exhibited a nonoverlapping enrichment for both mature and early markers (Fig. 3B), confirming the presence of multiple stages of B cell development in these niches.

Next, we reclustered all B cells from the three tissues on a single UMAP space (Fig. 3C) and found that B cells from the BM and dura occupied overlapping territories, whereas most of the blood B cells clustered separately (Fig.

3D). This analysis yielded 10 different clusters (C0 to C9). C0 and C5 were almost entirely (>90%) formed by blood B cells; C3, C6, C8, and C9 contained B cells from both BM and dura but were largely depleted of blood B cells (<5%); C1 and C4 contained B cells from both blood and dura but were depleted of BM B cells (<5%); and C2 and C7 contained B cells from all compartments (Fig. 3E). To determine the identity of each cluster, we performed a differential gene expression analysis (cluster versus total; cutoff = $\log_2FC > 0.5$ where FC is fold change) (Fig. 3F and table S1), followed by enrichment analysis of Gene Ontology (GO) biological process (fig. S8, A and B). From these analyses, we determined that blood contained primarily mature naïve B cells (C0, C1, C2, C5; fraction F), a small subset of immature B cells (C4; fraction E), and B1b cells (C7). By contrast, BM and dura contained mature naïve B cells (C2; fraction F), immature B cells (C6; fraction E), pre-B cells (C3; fraction D), pro-B cells (C9; fraction B-C), and mitotic B cells (C8). B cell receptor sequencing (BCR-seq) analysis showed that 88.1% of dura B cells with

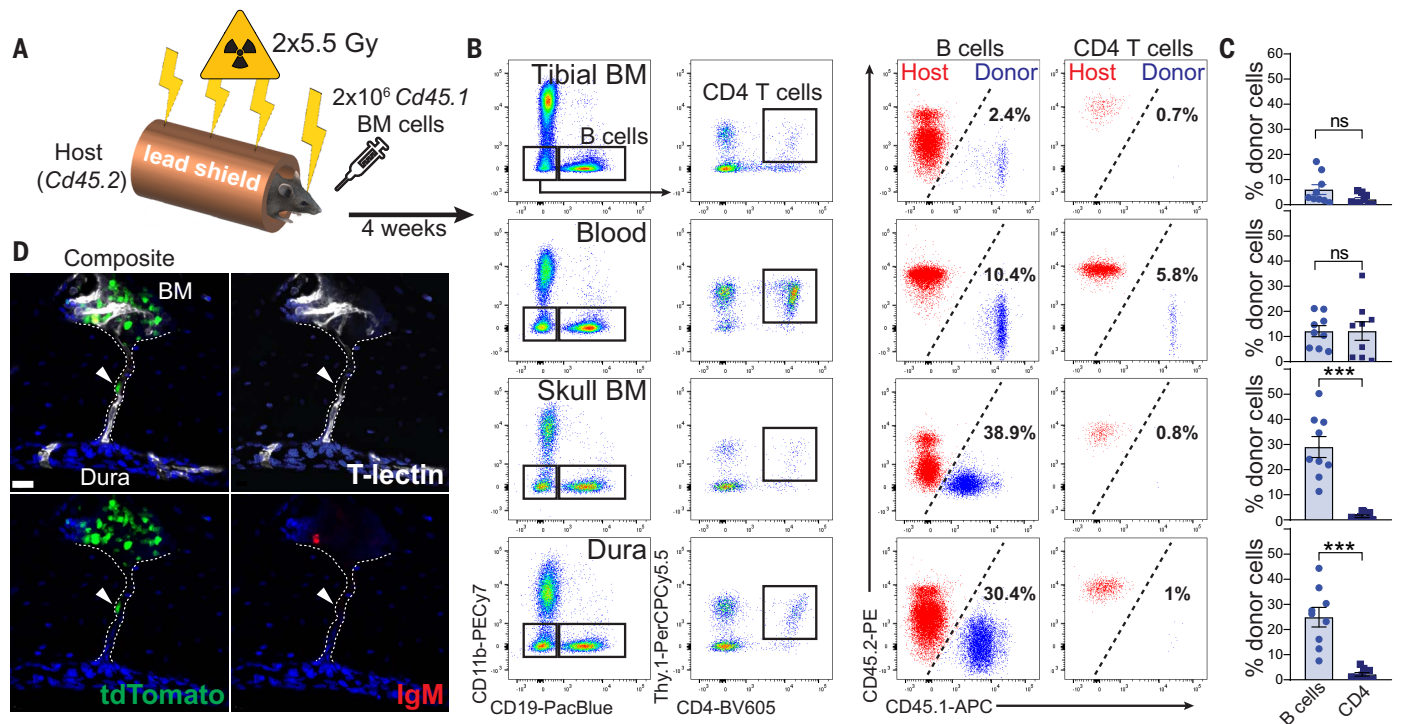


Fig. 5. Skull BM chimeras demonstrate that dura B cells originate from the calvaria. (A) Schematic depiction of the experimental design of calvaria BM transplantation. (B) Representative flow cytometry plots of B cells (gated on CD19⁺CD11b⁻ cells) and CD4 T cells (gated on CD19⁻CD11b⁻Thy.1⁺CD4⁺ cells) from multiple compartments in recipient mice (left). The percentages of donor-derived (CD45.1⁺) B and CD4

T cells are shown (right). (C) Frequency of donor-derived B cells and CD4 T cells per compartment (mean ± SEM; n=9 mice; Mann-Whitney U test ***P<0.001; data generated from two independent experiments). (D) Representative confocal image of an IgM⁺ B cell trafficking from the calvarial BM toward meninges through a skull vascular channel (white arrowhead) (scale bar: 20 μm).

productive V(D)J rearrangement were IgM type, again confirming their early stage of development (Fig. 3G). Finally, we performed pseudotime analysis (Fig. 3H) and identified a developmental trajectory that originated from mitotic B cells, then traversed pro-B and pre-B intermediate stages, before eventually giving rise to mature B cells (Fig. 3I). To empirically test this model, we performed bromo-deoxyuridine (BrdU) pulse-chase experiments focusing on BM and dura B cells (fig. S8C). At 24 hours post-BrdU pulse, early B cells exhibited the maximal incorporation of BrdU. At 3 days, the percentage of BrdU⁺ early B cells was sharply reduced, but it increased in both late and mature B cell populations. At 5 days, almost no BrdU⁺ B cells could be detected, presumably because BrdU-labeled cells underwent apoptosis, further differentiated, or were progressively diluted by newly generated B cells. Thus, the molecular signature of dura B cells highlights a stepwise developmental continuum, comprehensive of multiple intermediate phenotypes that are normally found in the BM but not in the periphery.

To validate the scRNA-seq data, we performed a mass cytometry study of dura, blood, and BM B cells (Fig. 4A and fig. S9). Unsupervised clustering of the CD45⁺CD19⁺ popula-

tion using t-distributed stochastic neighbor embedding (t-SNE) identified seven distinct clusters (C1 to C7) (Fig. 4B and table S2). We analyzed clusters C1 to C6 in detail (Fig. 4, C and D), whereas C7 was excluded from further analysis because it contained only 17 cells. C1 and C4 exhibited a typical mature phenotype (MHC-II⁺IgM⁺IgD⁺) but differentially expressed κ or λ light chains. C2 and C5 had an immature B cell phenotype (IgD^{lo}CD22^{lo}CD21^{lo}CD23^{lo}CD24⁺), whereas κ or λ light chains were differentially expressed. C3 had an early B cell phenotype (IgD⁻CD21⁻CD23⁺IgM^{lo}CD24⁺CD43⁺IL7R⁺CD93⁺). C6 was negative or low for both naïve B cell markers and pre-B markers but expressed CD43, CD44, CD73, and PD-L1, indicating an activated phenotype (16). Next, we determined the distribution of B cells from each compartment among the six clusters (Fig. 4E). Blood B cells were maximally enriched in C1 (88.6%), BM B cells were distributed among all clusters (C1= 49.6%, C2 = 13%, C3 = 30.7%), and dura B cells were primarily concentrated in C2 (44.3%), with substantial fractions in C1 (18.8%) and C3 (22.6%). Blood and BM were equally represented in C4 (5.4 and 4.1%, respectively), whereas the dura was more abundant than either blood or BM in C5 (6.9% versus 1.3 and 1.9%). Thus, mass cytometry analysis confirms

that the dura mater contains a large proportion of developing B cells.

Meningeal B cells mostly originate from the calvaria

Because only a few immature B cells were present in the blood, it was unlikely that developing B cells in the dura originated from the systemic circulation. We hypothesized that dura B cells originated in the calvarial BM. Indeed, the caudal region of the skull harbored a large hematopoietic niche (fig. S10, A and B), containing a variety of immune cells, including IL7R⁺ early B cells and LSK stem cells (fig. S10C). Electron microscopy (EM) and confocal imaging highlighted a complex cellular system in this area, containing both myeloid and lymphoid cells (fig. S10, D and E). To test our hypothesis, we performed an atypical BM transplantation experiment. During irradiation, the mouse body was protected with a lead shield, leaving only the head fully exposed (Fig. 5A). Head-irradiated Cd45.2 mice received Cd45.1 BM cells and 4 weeks later, the percentage of B cell chimerism was assessed in different tissues (Fig. 5, B and C). In both tibial BM and peripheral blood, only a negligible percentage of donor-derived B cells was found (6 and

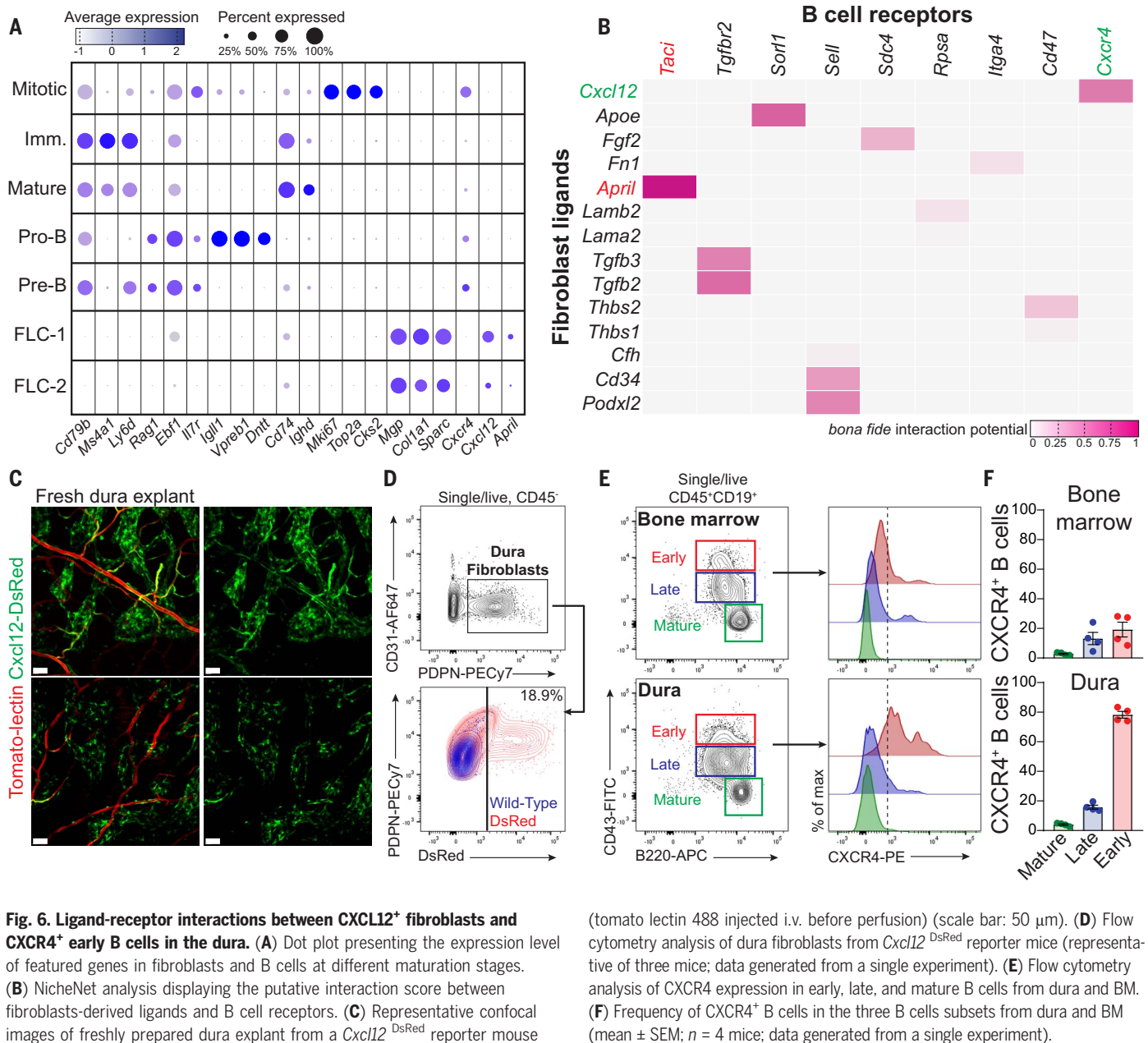


Fig. 6. Ligand-receptor interactions between CXCL12⁺ fibroblasts and CXCR4⁺ early B cells in the dura. (A) Dot plot presenting the expression level of featured genes in fibroblasts and B cells at different maturation stages. (B) NicheNet analysis displaying the putative interaction score between fibroblasts-derived ligands and B cell receptors. (C) Representative confocal images of freshly prepared dura explant from a *Cxcl12*^{DsRed} reporter mouse

12.1% respectively), whereas a large population of donor-derived B cells was present in skull BM and dura (29 and 24.9%, respectively). By contrast, almost no donor-derived CD4⁺ T cells were found in these compartments. We performed the reverse experiment, using a *Cd45.1* host, transplanted with *Cd45.2* BM cells and obtained comparable results (fig. S11A). To determine whether circulating B cells may potentially contribute to the pool of meningeal B cells under homeostasis, we performed a parabiosis experiment using wild-type and CD19-Tomato mice. After 4 weeks of shared circulation, the percentage of tdTomato-positive B cells was assessed in wild-type mice. A large population of parabiont-derived B cells

was present in the blood and spleen (39.2 and 36.4%, respectively), whereas a minor infiltration could be found in brain and dura (11.3 and 8.0%, respectively) (fig. S11, B and C). Comparable results were obtained by adoptive transfer of CD19-Tomato splenocytes into wild-type recipient mice (fig. S11, D and E). Thus, most meningeal B cells appear to originate in the calvarial BM and not from the circulation.

It has been recently shown that vascular channels form a direct communication between the calvaria and the meningeal space, thus allowing migration of immune cells independently of the systemic circulation (4, 6). We performed confocal imaging of skull cryosections after immunofluorescent staining for

endothelial markers (tomato lectin, CD34, and CD31). B cells were visualized by means of the CD19-Tomato reporter. In agreement with these studies, we found vascular channels through the inner skull bone (fig. S12A). As a complementary technique, we performed x-ray tomography on intact skull specimens impregnated with radiopaque metals. The resulting three-dimensional (3D) image displayed in *z* series reveals the presence of radiolucent areas (seemingly vessels) running through the calvaria and opening at the base of the sagittal sinus (fig. S12b and movie S2). Finally, we provide evidence of IgM⁺ B cells trafficking through these channels, confirming that calvaria-derived B cells reach the meningeal compartment at an early stage of

their development (Fig. 3D and fig. S12, C and D).

Dural fibroblasts produce crucial factors for B cell development

Notably, one of the top signature genes of fibroblast-like cells (FLCs) in the dura was *Cxcl12* (17), whereas dural early B cells expressed *Cxcr4* (Fig. 6A). NicheNet analysis highlighted a network of molecular communications between FLC and dura B cells. Among the several ligands detected in dural fibroblasts, *Cxcl12*, *April*, *Tgfb2*, and *ApoE* were assigned a high probability score (Fig. 6B). *Cxcl12* expression in dural FLCs was confirmed by imaging and flow cytometry using *Cxcl12*^{DsRed} reporter mice (Fig. 6, C and D). Surface expression of CXCR4 in early B cells was also confirmed by flow cytometry (Fig. 6E). The majority of early B cells in the dura had CXCR4 expressed on the cell surface (Fig. 6F), suggesting that calvaria-derived B cells may require this receptor for their homing to the meningeal compartment. Finally, confocal imaging demonstrated B cells in close contact to *Cxcl12*-expressing FLCs in the sagittal sinus (fig. S13). As the CXCL12–CXCR4 axis is crucial for B cell development, we propose that dural FLCs may support the survival and differentiation of early B cells derived from the calvarial BM.

ABCs and plasma cells accumulate in mouse meninges during aging

Lymphocytes exhibit clonal and phenotypical imbalance during aging (18, 19). Indeed, we found a marked increase in the total number of B cells in the dura of aged mice (fig. S14, A and B). We then investigated the impact of aging on meningeal B cells by comparing young (8- to 12-week-old) and aged (20- to 25-month-old) mice by scRNA-seq and scBCR-seq (Fig. 7A). An accumulation of clonal B cells was found in the aged dura (fig. S14C), as well as an increased clonal overlap with blood B cells (fig. S14D), suggesting infiltration from the periphery. All B cell clusters in the dura were equally represented in young and aged mice, except for one cluster that was almost entirely (96.1%) derived from aged mice (Fig. 7, B and C) and was therefore annotated as “age-associated B cells” (ABCs). Differential gene expression analysis between ABCs and mature B cells ($\log_2FC > 0.5$; adjusted $P < 0.01$) revealed 105 differentially expressed genes (table S3). The top up-regulated transcripts included *ApoE*, *Ly6a*, *Ighm*, *Igkc*, *Cd2*, *Lgals1*, *Zbtb20*, and *Sytk*, whereas the top down-regulated transcripts contained *Fcer2a*, *Cr2*, *Cd55*, *Sell*, and *Ebfl* (Fig. 7, D and E). Using flow cytometry, we confirmed a significant expansion of B220^{hi}CD23[−]CD2⁺Sca1⁺ ABCs in the dura of aged mice (Fig. 7, F and G). Consistent with the scRNA-seq data, this cell population also

expressed increased amounts of Syk and ApoE protein (Fig. 7H and fig. S14E). Furthermore, dura ABCs had increased numbers of *Ighm* heavy-chain transcripts compared to mature B cells (Fig. 7I). scBCR-seq further confirmed increased *Ighm*, and reduced *Ighd*, C-region usage in ABCs (Fig. 7J). Additionally, ABCs exhibited greater similarity in their V gene usage profiles (fig. S14F), as well as accumulation of somatic mutations in the BCRs of cells expressing the *Ighm* heavy chain (fig. S14G). Thus, dural ABCs are antigen-experienced B cells. Using these BCR data, we determined the percentage of B cells in clones that were shared between dura and blood (Fig. 8A). We found that dural B cells had no clonal overlap with circulating B cells in young mice, whereas a minor overlap could be observed in aged mice. By contrast, many dural ABCs were members of clones shared with the blood (30.8%), suggesting that these cells had trafficked from the periphery.

Next, we focused on dural plasma cells (fig. S15, A and B), which also appeared expanded in the aged dura (Fig. 7C). Differential gene expression analysis revealed that the expression of Ig isotypes was markedly shifted between the two age groups. In young mice, dural plasma cells were predominantly IgA⁺ but became mostly IgM⁺ in aged mice (fig. S15C). By confocal imaging, we surveyed plasma cells located along the sagittal sinus (fig. S15D) and confirmed the massive increase in the number of these cells in aged mice (fig. S15E), especially IgG and IgM types, whereas the number of IgA plasma cells was unchanged (fig. S14F). Lastly, we assessed the redundancy of plasma cell clones detected by scBCR-seq to gain insight into their origin (Fig. 8B). Although only a few plasma cell clones could be detected in the dura mater of young mice, we found an important clonal overlap with blood, indicating that plasma cells (mostly IgA) from young mice infiltrate the dura from the periphery, as recently demonstrated (20). By contrast, plasma cell clones in the aged dura (mostly IgM) exhibited a negligible overlap with the blood repertoire, indicating that most of these cells were not derived from the blood. Notably, we found a clonal overlap (15.4%) between dural plasma cells and dural ABCs, suggesting that, in aged mice, some dural ABCs may locally undergo terminal differentiation into IgM-secreting plasma cells. The top 10 most expanded clones detected in the aged dura specifically mapped onto both ABC and plasma cell clusters (Fig. 8C), supporting the possibility of a clonal relatedness between these two populations.

Discussion

Recent studies have shed light on the origin and phenotypic diversity of the myeloid cell landscape at the CNS borders (8, 21–24). Yet,

little is known about B cells resident at CNS interfaces. Using complementary techniques, we demonstrated that meningeal B cells encompass multiple stages of the development. These B cells originate in the calvaria and infiltrate the meninges through a network of channels uncoupled from the systemic circulation. Early B cells may complete their maturation within the meningeal compartment, wherein dura fibroblasts can provide critical molecules for B cell development, such as CXCL12 (25, 26). Using *Nur77*^{GFP} mice, in which green fluorescent protein (GFP) expression reflects BCR engagement by self-antigens (27), we showed that transitional and mature meningeal B cells are equipped with a functional BCR, evinced by GFP expression in these populations (fig. S16, A to C). Thus, the calvaria may provide an early and rapid source of B cells that develop in the dura, resulting in negative selection of B cells with high affinity for local self-epitopes. In support of this hypothesis, transgenic mice carrying the IgH chain of the mAb 8.18C5 specific for myelin oligodendrocyte glycoprotein (MOG) (28) showed a significant reduction of MOG-specific B cells in dura compared to tibial BM, suggesting that negative selection may occur locally (fig. S16, D to F). The calvaria was recently described as a source of meningeal neutrophils (4), and a companion paper shows that calvarial BM supplies the CNS with myeloid cells, both under homeostasis and inflammation (29). We further integrate these findings showing that meningeal B cells share a similar origin.

In aged mice, we identified a distinct population of meningeal B cells corresponding to ABCs (30), which have been mostly found in the spleen (19, 31–33), but never in the CNS. scBCR-seq indicates that dural ABCs are antigen-experienced B cells infiltrated from the systemic circulation. Additionally, the aged dura mater features a robust expansion of IgM⁺ and, to a lesser extent, IgG⁺ plasma cells. By contrast, meningeal IgA⁺ plasma cells, which derive from the gut (20, 34), appeared unaffected by aging. The infiltration of blood-borne ABCs, as well as the accumulation of plasma cells within the meninges, may endanger the immune-privileged CNS environment during aging. Because B cells are key players in neuroinflammatory and autoimmune disorders (35, 36), these findings may help better explain the origin of self-reactive B cells in these pathologic conditions.

Materials and methods

Animals

All mice used in this study were C57BL/6J housed under specific pathogen-free conditions at Washington University School of Medicine animal facility. Homozygous *Cd19*^{Cre} mice were

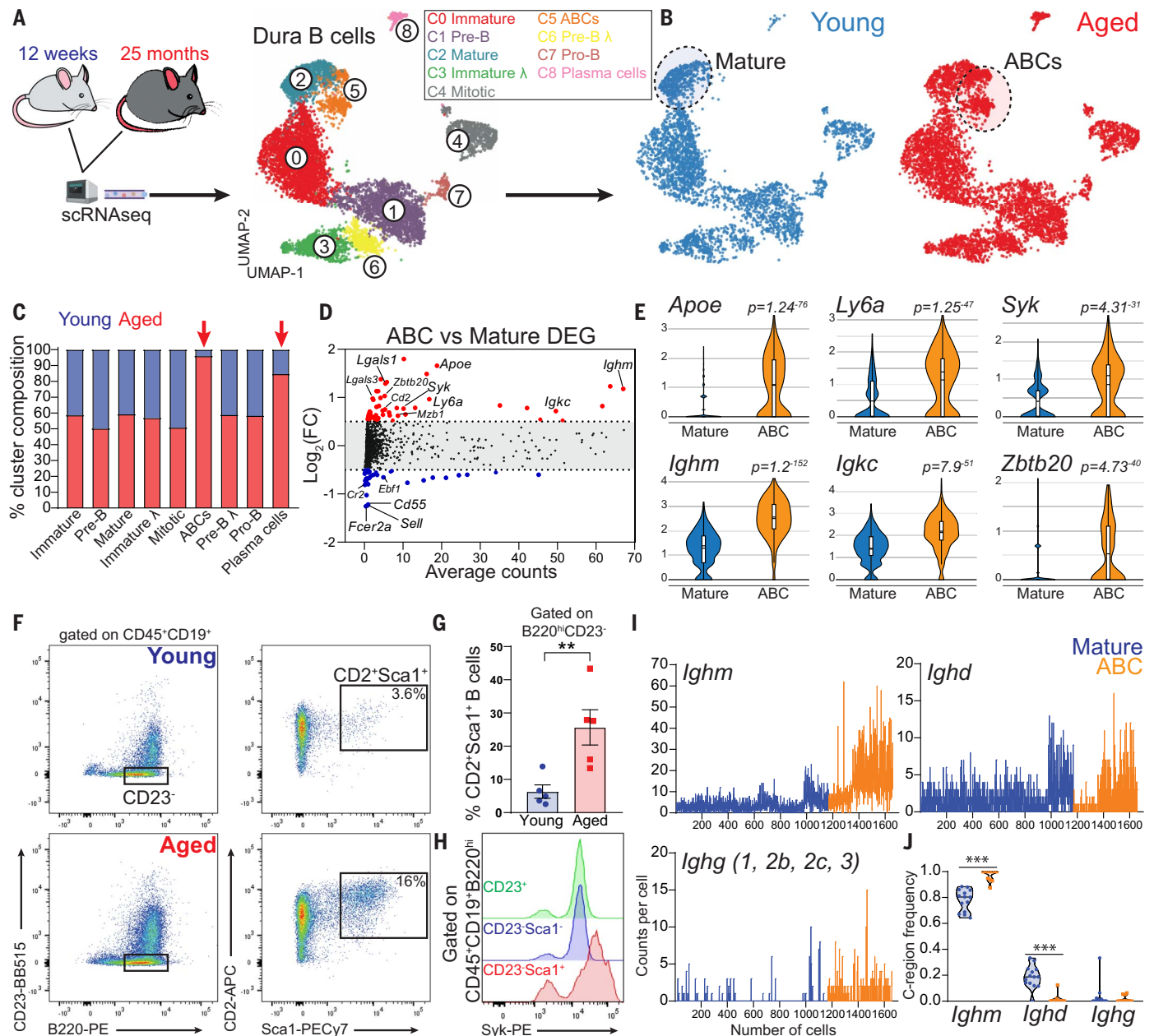


Fig. 7. Age-associated B cells disseminate throughout the dura of aged mice. (A) Schematic depiction of the experimental design of scRNAseq comparing young and aged mice. UMAP of 9352 B cells aggregated from seven 12-week-old and seven 25-month-old C57BL6 female mice (data generated from two independent experiments). (B) Distribution of B cells from young and aged mice. (C) Contribution of young versus aged mice to each cluster. (D) Differential gene expression analysis of ABCs versus mature B cells. (E) Violin plots showing top up-regulated genes in ABCs compared to mature B cells. (F) Dura ABCs gated as the B220^{hi}CD23⁻CD2⁺Sca1⁺ cells. (G) ABC

population is significantly increased in the dura of aged mice compared to young mice (mean \pm SEM; $n = 5$ mice; unpaired Student's t test, $**P < 0.01$; data generated from two independent experiments). (H) Flow cytometry histogram showing increased amounts of Syk protein in dura ABCs (representative of three 18-month-old female mice; data generated from a single experiment). (I) Ig heavy-chain transcript counts per cell in ABCs and mature B cells. (J) Frequency of heavy-chain usage determined by BCRseq in ABCs and mature B cells (violin plot; $n = 11$ to 14 mice per group; two-way ANOVA and Bonferroni post-hoc test $***P < 0.001$).

purchased from the Jackson Laboratory (JAX stock #006785) and mated with homozygous *Rosa26-STOP^{fl}Tomato* (Ai14) mice bred in house. Heterozygous *Cxcl12^{DsRed}* mice were purchased from the Jackson Laboratory (JAX stock #022458) and mated with C57BL/6J mice bred in house. *Nur77^{GFP}* mice were provided

by Dr. P. Allen (Department of Pathology and Immunology, Washington University School of Medicine). *IGH^{M0G}* mice were provided by Dr. G.F. Wu (Department of Neurology, Washington University in Saint Louis). All experiments involving laboratory animals were performed under the approval of the

Institutional Animal Care and Use Committee at Washington University in St. Louis (protocol #19-0981). For flow cytometry and imaging experiments, both sexes were used and equally distributed among the experimental groups. For CyTOF, scRNAseq, and parabiosis experiments, females only were

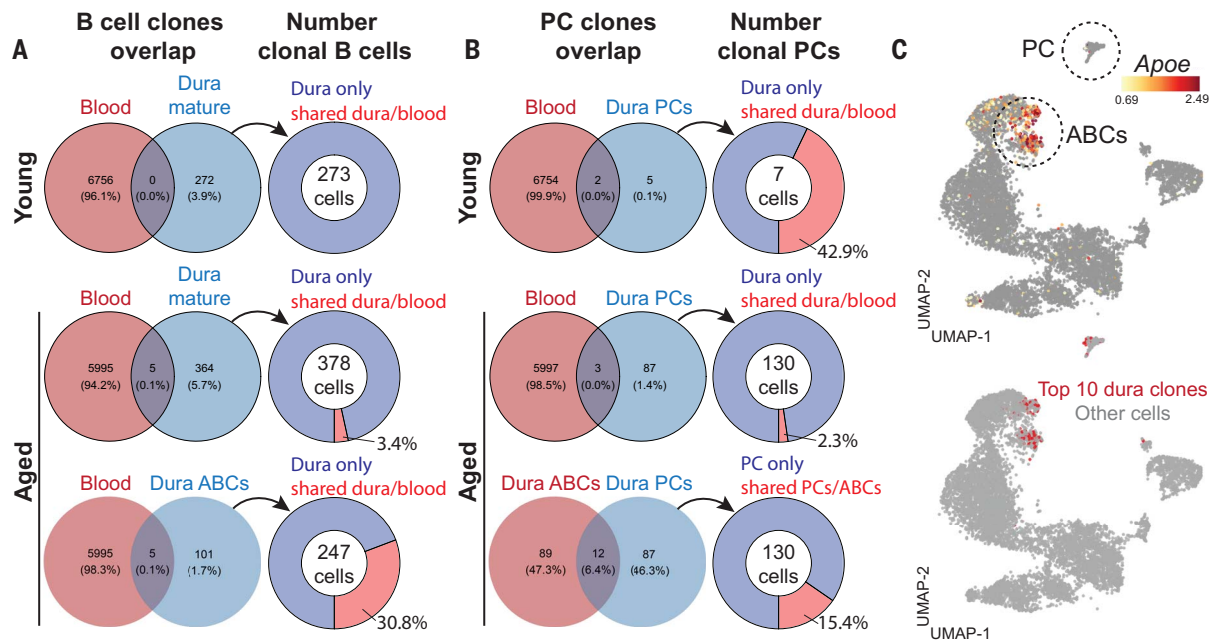


Fig. 8. Age-associated B cells in the aged dura originate from the periphery. (A) Venn diagrams representing the proportion of detected B cell clones shared between dura mature B cells and blood in young and aged mice, or between dura ABCs and blood. The connected pie chart represents the percentage of dura B cells (mature or ABCs) belonging to shared clonotypes. (B) Venn diagrams representing the proportion of detected plasma cell (PC) clones shared between dura and blood in young and aged mice, or between dura plasma cells and dura ABCs. The connected pie chart represents the percentage of dura plasma cells belonging to shared clonotypes. (C) UMAP showing the distribution of the 10 most frequent clones in the dura.

used to minimize biological variability. For studies on young-adult mice, 8- to 12-week-old mice were used. For studies on aged mice, 20-25-month-old mice were used. On the day of sacrifice, mice received a lethal dose of ketamine-xylazine injected intraperitoneally (i.p.) (respectively, 300 mg and 30 mg per kilogram of body weight). After complete loss of the paw-pinch reflex, blood samples were collected by heart puncture. All other tissues analyzed in this study (dura, brain, spleen, and bone marrow) were collected upon perfusion with 30 ml of ice-cold phosphate-buffered saline (PBS). Parabiotic mice were prepared by the surgery core in the Hope Center for Neurological Disorders (Washington University, St. Louis, MO) as previously described (37).

Intravenous injection of CD19-Tomato splenocytes

Five-month-old CD19-Tomato mice were sacrificed with CO₂ and spleens were immediately collected into ice-cold PBS. Splenocytes were mechanically extracted by mashing the spleen on a 70- μ m strainer and collected in a 50-ml conical centrifuge tube. Samples were pelleted by centrifugation at 300g for 15 min at 4°C, followed by red blood cells lysis on ice for 2 min. Splenocytes were then washed in sterile PBS, pelleted by centrifugation at 300g for 5 min at 4°C, and resuspended in 1 ml of sterile PBS. Before counting, cells were filtered

through a 35- μ m sterile strainer. Three-month-old gender-matched C57BL/6 mice were used as recipients. Mice were anesthetized with a dose of 80 mg per kilogram ketamine and 10 mg per kilogram xylazine administered by i.p. injection. After complete loss of the paw-pinch reflex, mice received a retro-orbital injection of 2×10^7 freshly prepared splenocytes from CD19-Tomato mice. Recipient mice were sacrificed one week later and blood, spleen, brain, and dura were analyzed by flow cytometry.

Intra cisterna magna injection of CD19-Tomato splenocytes

A single CD19-Tomato mouse was perfused under sterile conditions and spleen was immediately collected into ice-cold PBS. Splenocytes were mechanically extracted by mashing the spleen on a 70- μ m strainer and collected in a 50-ml conical centrifuge tube. Samples were pelleted by centrifugation at 300g for 15 min at 4°C, followed by red blood cell lysis on ice for 2 min. Splenocytes were then washed, and resuspended in sterile PBS at a final concentration of 5×10^5 cells/ μ l. Injection of 2.5×10^6 CD19-Tomato splenocytes (5 μ l) in the cisterna magna of 3-month-old gender-matched C57BL/6 mice was performed as previously described (10). After injection, mice were sutured and monitored until they completely recovered. The dura mater, cervical lymph nodes, and inguinal lymph nodes were collected 24 hours after injection.

Sample preparation for flow cytometry or scRNAseq

Blood samples underwent red blood cell lysis at room temperature for 5 min. Hereafter, sample preparation was entirely carried out either on ice or at 4°C. No enzymatic digestion was used in this study. The dura mater was stripped off the inner skull surface using precision tweezers. Single-cell suspensions of brain, dura, and calvarial bone marrow were generated via mechanical dissociation using a dounce homogenizer. Cells were then filtered through a 70- μ m strainer and collected in a 50-ml conical centrifuge tube. Splenocytes were mechanically extracted by mashing the spleen on a 70- μ m strainer and collected in a 50-ml conical centrifuge tube. Tibial bone marrow was extracted from open tibias into a 1.5-ml microcentrifuge tube by centrifugation at top-speed for 20 s using a bench centrifuge. Spleen and bone marrow samples underwent red blood cells lysis on ice for 2 min. Samples were pelleted by centrifugation at 300g for 15 min at 4°C. Dura pellets were resuspended in 5 ml of 75% isotonic percoll, overlaid with 3 ml of PBS. Stromal cells and debris were depleted by centrifugation at 1000g for 30 min at 4°C (acceleration 0, break 1). The interface percoll-PBS was collected for analysis. Brain pellets were resuspended in 5 ml of 30% isotonic percoll, overlaid with 2 ml of PBS. Myelin was depleted by centrifugation at 1000g for 30 min

at 4°C (acceleration 0, break 1). The pellet was collected for analysis.

Flow cytometry analysis

Single-cell suspensions were washed in PBS followed by live/dead staining (Zombie Aqua or Zombie UV, Biolegend) at 1:1000 dilution for 15 min on ice. Fc-receptor blockade was performed using CD16/32 blocking antibody (clone 93, Biolegend; or clone 197, made in house) incubated 10 min on ice. Surface staining was always performed between 30 min and 1 hour on ice (complete antibody list in table S4). For staining of intracellular markers, fixation and permeabilization were performed using either the BD Cytofix/Cytoperm kit (BD Bioscience), or the Fcγ3/Transcription Factor Staining kit (eBioscience), according to the product instructions. For ApoE intracellular staining, 1 mg/ml of purified anti-ApoE (clone HJ6.3, kindly provided by David Holtzman) was conjugated with AlexaFluor647 and fixed/permeabilized cells were stained overnight (1:100 dilution) at 4°C. For staining of IGH^{MOG} BCR, B cells were incubated with 2 mg/ml of biotin-conjugated recombinant MOG (1:100 dilution) for 30 min on ice prior to surface markers staining. Flow cytometry analysis was performed on BD X20, BD LSR Fortessa, or BD Canto-II (BD Bioscience). Raw data were analyzed with FlowJo v10.

Skull bone marrow transplantation

Twelve-week-old C57BL/6J (*Cd45.2*) mice were anesthetized with a dose of 80 mg per kilogram ketamine and 10 mg per kilogram xylazine administered by i.p. injection. Mice were inserted into a 1-inch-thick lead shield (1 inch-thick Lead Vial Shield, 50 ml, Pinestar Technology) leaving only the head exposed. Each mouse received 11 Gy of gamma irradiation, split into two doses 4 hours apart. Immediately after the second dose, mice were reconstituted with 2×10^6 *Cd45.1* bone marrow cells injected intravenously (i.v.) Mice were left undisturbed in their home cage for the following 4 weeks. On the day of experiment, samples were processed as described above. The percentage of chimerism within different immune populations was determined by staining for CD45.2 and CD45.1.

Immunofluorescence staining

Brains, spinal cords, and skull caps were fixed in 4% paraformaldehyde (PFA) at 4°C overnight. Fixed specimens were then dehydrated in 30% sucrose solution for at least 48 hours and then cut into 60- to 100-μm-thick sections at the cryostat (Leica). Staining on free-floating sections was performed. Cryosections were blocked for 4 hours in PBS with 5% bovine serum albumin (BSA) and 0.5% Triton X-100. Primary antibody staining was performed in PBS with 1% BSA and 0.5% Triton

X-100 for 48 hours at 4°C. Secondary staining with fluorochrome-conjugated antibodies was performed at room temperature for 2 hours (complete antibody list in table S4). Immunostained sections were mounted on Superfrost glass slides (Fisher Scientific) and embedded in Prolong Glass anti-fade mounting media (ThermoFisher). Lymph nodes were fixed and dehydrated as above and sliced into 20 μm-thick sections at the cryostat. Sections were directly mounted on the Superfrost glass slides and air dried. Blocking was performed for 1 hour (5% BSA, 0.5% Triton X-100), and antibody staining for 24 hours at 4°C (1% BSA, 0.5% Triton X-100). For whole-mount preparation of dura mater, skull caps were fixed as above, and then decalcified in 0.5 M pH 8.0 EDTA solution (Corning) for 48 hours at 4°C. Blocking and staining were performed as above. The whole skull was mounted on Superfrost glass slides and embedded in Fluoromount-G anti-fade mounting media (Southern Biotech). Stained samples (both cryosections and whole mount preparations) were covered with 1.5H high-precision cover glass (Marienfeld Superior) and left to dry overnight at room temperature before imaging.

Confocal imaging

Confocal imaging of dura mater whole mounts preparations and brain cryosections was performed using a Zeiss LSM880 airyscan inverted confocal microscope equipped with a 34-channel GaAsp (gallium arsenide phosphide) detector. Cryosections were imaged with a 40×/1.4 oil-immersion objective. Dura whole mounts were imaged with a 40×/1.2 water-immersion objective. Images were acquired at 2048 × 2048-pixel resolution, 20- to 50-μm-thick *z*-stack *z*-step = 1 μm, line averaging = 2, using ZEN Black (ZEISS Efficient Navigation) software (Zeiss). When needed, tile-scan mode was used to generate large filed-of-view images. Confocal imaging of leptomeninges was performed on fresh unfixed brains from young adult *CD19^{Cre}; Rosa26^{tdTomato}* mice. Briefly, mice were anesthetized with a lethal dose of ketamine and xylazine administered by i.p. injection. After complete loss of the paw-pinch reflex, blood vessels were fluorescently labeled by retro-orbital injection of 100 μl of DyLight 488-labeled tomato lectin (Vector Laboratories, 1:1 dilution). Two minutes later, the mouse was decapitated, and the brain was immediately rinsed in ice-cold PBS and imaged using a Leica SP8 inverted confocal microscope. Images were acquired with a 25×/0.95 water-immersion objective, at 2048 × 2048- or 4096 × 4096-pixel resolution, 70 μm-thick *z*-stack, *z*-step = 5 μm, line and frame average=3, using Leica Application Suite, LAS X (Leica Microsystems). Maximal projections were rendered in Imaris V8.3 (Bitplane, Zurich, Switzerland).

Two-photon imaging

Young adult *CD19^{Cre}; Rosa26^{tdTomato}* mice were anesthetized with a dose of 80 mg per kilogram ketamine and 10 mg per kilogram xylazine administered by i.p. injection. After complete loss of the paw-pinch reflex, fur on the head and neck was shaved and the skin on the parietal skull bone was surgically removed. Skull bone was thinned using an electrical micro drill and the head was fixed on a metal holder to minimize movements during the live imaging. Immediately before imaging, blood vessels were fluorescently labeled by retro-orbital injection of 100 μl of DyLight 488-labeled tomato lectin (Vector Laboratories, 1:1 dilution). Time-lapse in vivo imaging was performed with a Leica SP8 2-photon imaging system. DyLight-488 and tdTomato were excited with Mai Tai Deepsee and Insight Deepsee lasers (Spectra Physics, Santa Clara Ca, USA) optimally tuned to 920 nm and 1050 nm respectively. Emission spectra were collected on ultrasensitive hybrid detectors as follows: >560 nm (tdTomato), 495-560 nm (DyLight 488), and <458 nm (second harmonic). The subdural space was identified using the second harmonic generation and the blood vessels as territory landmarks. Time-lapse imaging was performed with a 25×/0.95 water-immersion objective, at 1024 × 1024-pixel resolution, *z*-stacks = 40 μm, *z*-step = 2.5 μm, acquisition speed = 4 frames per min, imaging time = 30 min, using Leica Application Suite, LAS X (Leica Microsystems). Maximal projection and video editing were performed with Imaris V8.3 (Bitplane, Zurich, Switzerland).

Mass cytometry (CyTOF) analysis

Single-cell suspension from dura mater, tibial bone marrow and blood were obtained as described above. Cells were resuspended in Cy-FACS buffer (PBS, Rockland; 0.1% BSA, Sigma A3059; 0.02% NaN₃; 2mM EDTA). Fc-receptor blockade was performed using CD16/32 blocking antibody (clone 93, Biolegend, 1:100). Cell were stained for 1 hours on ice with the surface staining cocktail (complete antibody list in table S4). Viability staining was performed by resuspending cells in 2.5 μM Cisplatin for 1 min. Cells were then fixed with 4% PFA for 30 min on ice followed by overnight DNA staining with iridium-labeled intercalator (1:3000). Cells were acquired with the CyTOF2 mass cytometry system (Fluidigm) and analyzed using Cytobank. Immune cells were hierarchically gated as follows: nucleated cells, exclusion EQ calibration beads, live cells, single cells, and CD45⁺. Dimensionality reduction analysis was performed on CD45⁺ cells using the viSNE toolX in Cytobank to apply the Barnes-Hut implementation of the t-SNE algorithm. Unsupervised clustering of the total CD45⁺ cells was performed using the following parameters: iterations = 2000;

perplexity = 100; Theta = 0.5. This setup has been chosen as it demonstrated to produce the best separation of biologically meaningful populations in the three compartments. Next, the CD45⁺CD19⁺ population from the blood, BM, and dura were further analyzed with FlowJo v10. B cells populations from independent replicates were aggregated and down-sampled to 2000 single/live B cells per compartment. Finally, downsampled files were concatenated and reclustered by t-SNE algorithm using default settings (iterations = 1000; perplexity = 20; Theta = 0.5).

BrdU staining for cell proliferation

Mice received two i.p. injections 6 hours apart of 5 mg BrdU (Sigma) dissolved in PBS. Mice were randomized and sacrificed at multiple time points after injection (24 hours, 3 days, 5 days, and 7 days). Samples were prepared as described above, followed by BrdU staining using the BrdU flow Kit (BD Pharmingen). Briefly, after surface staining, cells were fixed with fix/perm BD buffer for 20 min on ice, followed by 10 min nuclear permeabilization with BD perm-plus buffer, and a second fixation for 5 min at room temperature. Fixed/permeabilized cells were incubated with deoxyribonuclease I (DNase I) (300 µg/ml) for 1 hour at 37°C, followed by intranuclear BrdU staining (Biolegend clone 3D4, 5 µl BrdU-PE per sample) for 30 min at room temperature. Flow cytometry analysis was performed on BD LSR Fortessa.

Transmission electron microscopy

After perfusion with ice-cold PBS, skull caps were removed and fixed with 4% paraformaldehyde (PFA), 0.1% glutaraldehyde (Polysciences Inc., Warrington, PA) in phosphate-buffer 0.1 M, pH 7.2 overnight at 4°C. Samples were decalcified in 0.5 M pH 8.0 EDTA solution (Corning) for 48 hours at 4°C and fixed again in 2% PFA, 2.5% glutaraldehyde in 100 mM sodium cacodylate buffer, pH 7.2 for 2 hours at room temperature. Samples were washed in sodium cacodylate buffer at room temperature and postfixed in 2% osmium tetroxide (Polysciences Inc.) for 2 hours at room temperature. Samples were then rinsed extensively in dH₂O prior to en bloc staining with 1% aqueous uranyl acetate (Ted Pella Inc., Redding, CA) for 1 hour at room temperature. After several rinses in dH₂O, samples were dehydrated in a graded series of ethanol and embedded in Eponate 12 resin (Ted Pella Inc.). Thick sections of 400 nm were cut with a Leica Ultracut UCT ultramicrotome (Leica Microsystems Inc., Bannockburn, IL) and stained with 1% toluidine blue, 2% sodium borate. Brightfield images were acquired on a Zeiss AxioObserver D1 inverted microscope (Carl Zeiss Inc. Thornwood, NY) equipped with an AxioCam 503 color camera. Areas of interest were identified, and images were

acquired with 20×/0.5 and 40×/1.2 objectives. Ultrathin sections of 95 nm from the areas of interest were then collected on Cu grids, stained with uranyl acetate and lead citrate, and viewed on a JEOL 1200 EX transmission electron microscope (JEOL USA Inc., Peabody, MA) equipped with an AMT 8-megapixel digital camera and AMT Image Capture Engine V602 software (Advanced Microscopy Techniques, Woburn, MA).

X-ray tomography

Upon perfusion, mouse cranium was fixed in 4% PFA overnight at 4°C and stained with 10% Lugol's iodine solution (38) at 21°C for 5 days prior to imaging. Following incubation, samples were embedded in 2% agarose, and imaged using a Zeiss Versa 520 (Carl Zeiss Microscopy, White Plains, NY) using either a 0.4× flat panel detector or a 4× objective at 80 kV. Final tomograms were visualized, and resultant images were generated in Zeiss XM3DViewer v.1.2.9. Z-projections were generated in ImageJ.

Single-cell RNA sequencing and single-cell BCR sequencing library preparation

For scRNAseq seven 10-week-old and seven 25-month-old female mice were used. Single-cell suspension from dura mater, tibial bone marrow and blood were obtained as described above. No sorting or enrichment was used as this experiment aimed to achieve a comprehensive transcriptomic representation of both immune and stromal cells. Samples were resuspended into low binding microcentrifuge tubes with PBS + 0.04% BSA at a final concentration of ~1000 cells/µl. Single cells gene-expression and V(D)J libraries were prepared by the McDonnell Genome Institute (MGI) at Washington University using the 5' Single Cell with V(D)J Enrichment Reagents Kit from 10x Genomics. Using the 10x Chromium VDJ + 5' Gene expression v.1 platform, up to 17,500 cells were partitioned into nanoliter Gel-bead-in-Emulsions (GEMs) droplets. Each GEM underwent retro-transcriptase reaction to generate single-cell cDNA and received a unique 12-nt cell barcode and unique molecular identifier (UMI). GEM cDNA was amplified for 11 cycles before being purified using SPRiselect beads. For scRNAseq, 10 µl of purified cDNA was used to generate the library for RNA sequencing. Libraries were sequenced on a NovaSeq S4 (Illumina, 300 cycle kit) flow cell, targeting 50K read pairs per cell. For scBCRseq, 2 µl of purified cDNA was used to generate the sequencing of the V(D)J region. Sequencing was performed using a NovaSeq S4 (Illumina, 300 cycle kit) flow cell, targeting 5K read pairs per cell.

Single-cell RNAseq analysis

Cell Ranger Software Suite (v3.1.0) from 10X Genomics was used for sample demultiplex-

ing, barcode processing, and single-cell counting. Cell Ranger count was used to align samples to the reference genome GRCm38 (mm10), quantify reads, and filter reads and barcodes. Contamination by ambient RNA in droplets was normalized using SoupX (v1.4.5) (<https://github.com/constantAmateur/SoupX>). Furthermore, contaminating genes from erythrocytes and platelets (*Clu*, *Gng11*, *Gp1bb*, *Gp9*, *Hba-a1*, *Hba-a2*, *Hbb-b1*, *Hbb-b2*, *Nrgn*, *Pf4*, *Ppbbp*, and *Tubb1*) were filtered out from the dataset. The Seurat (v3.2.2) package in R was used for downstream analysis. For quality control, cells with mitochondrial content >20% were removed. Cells with low UMI and gene number per cell were filtered out. Cutoffs for UMI and gene number were determined on the basis of histograms showing cell density as a function of UMI per gene counts. For dura and bone marrow samples, cutoffs of >500 UMI and >250 genes were applied. For blood samples, cutoffs of >500 UMI and >1000 genes were applied. Genes expressed in fewer than 10 cells were removed from the dataset.

Samples from different tissues were clustered separately. For each tissue, data were normalized using the SCTransform method regressed on mitochondrial gene percentage and integrated using FindIntegrationAnchors function and Canonical Correlation Analysis (CCA) (39, 40). Principal component analysis was performed, and the top 40 principal components were selected for dimensionality reduction using the Uniform Manifold Approximation and Projection (UMAP) algorithm. For identification of marker genes and differential expression analysis, we used the MAST algorithm implemented through the Seurat R package (41). Marker genes were identified by comparing each cluster against all other clusters using the FindConservedMarkers function with default settings (log-fold change threshold of 0.25 and >10% cells expressing the gene) and age as the grouping variable. Cell clusters from each tissue were annotated based on marker gene expression and clusters consisting of doublets were manually removed. For further analyses of B cell heterogeneity, B cell clusters were extracted and re-clustered. For reclustering analyses, data were normalized using a scaling factor of 10,000 and mitochondrial read percentage was regressed with a negative binomial model. Principal component analysis was performed using the top 2000 most variable genes and UMAP analysis was performed using the top 10 principle components. Clustering was performed using a resolution of 0.4. For data visualization and figure preparation of scRNA-seq data BBrowser version 2.7.5 was used (42).

Single-cell pseudotime trajectories were inferred using diffusion map algorithms implemented through the R package destiny (43). Normalized expression values were used as

input for the generation of diffusion maps. Cells were ordered based on the first diffusion component. To further visualize B lineage differentiation, pseudotime was inferred using the slingshot R package (44). Gene Ontology analysis for biological processes enriched in different B cell populations was performed on the top 50 transcripts in each cluster using Metascape (<https://metascape.org>) (45). Receptor-ligand interactions were mined from the scRNA-seq data using the NicheNet algorithm (46). In brief, NicheNet analysis was performed using the marker genes for all clusters of dura B cell and dura fibroblast using default settings. After calculation of interaction scores between possible receptor-ligand combinations, pairs were filtered for those bona fide interactions that were documented in the literature and publicly available databases.

Single-cell BCR repertoire analysis

Sample demultiplexing and barcode processing was performed using the Cell Ranger Single-Cell Software Suite (10x Genomics). CellRanger-5.0.12 was used to align reads to the reference genome (vdj_GRCm38_alts_ensembl-5.0.0) and assemble BCRs. BCR sequencing data was processed using the Immcantation framework (imccantation.org) (47, 48). Germline V(D)J gene annotation was performed for all 10X Genomics BCR sequences using IgBLAST v1.16.0, with a curated set of Ig reference alleles specific for the C57BL/6 strain of *Mus musculus* (49). IgBLAST output was parsed using Change-O v0.4.6 (47). Additional quality control required sequences to be productively rearranged and have valid V and J gene annotations, consistent chain annotation (excluding sequences annotated with H chain V gene and L chain J gene), and a junction length that is a multiple of 3. Cells with exactly the same barcode and BCR sequences between different samples were excluded. Furthermore, only cells with exactly one H chain sequence paired with at least one L chain sequence were kept. After processing, there were 52,509 cells with paired H and L chains of which 19,447 had paired gene expression data.

B cell clonal lineages were inferred using hierarchical clustering with single linkage (50, 51). Cells were first partitioned based on common H and L chain V and J gene annotations and junction region lengths. Within each partition, cells whose H chain junction regions were within 0.07 normalized Hamming distance from each other were clustered as clones. This distance threshold was determined by manual inspection to identify the local minimum between the two modes of the bimodal distance-to-nearest distribution. The clones were further split based on the common L chain V and J gene.

Mutation frequency was calculated for cells by counting the number of nucleotide mis-

matches from the germline sequence in the H chain variable segment leading up to the CDR3. The calculation was performed using the *calcObservedMutations* function from *SHazaM* v1.0.2.

Statistical analysis

For flow cytometry and imaging data, graphs and statistics were produced using the GraphPad Prism 8 software package. Statistical difference between two groups was determined by either two-tailed unpaired Student's *t* test (when both groups passed the Kolmogorov-Smirnov normality test) or two-tailed Mann-Whitney *U* test (when at least one group did not pass the Kolmogorov-Smirnov normality test). When the effects of two independent variables were considered, the two-way analysis of variance (ANOVA) with Bonferroni post-hoc test was used. When more than two groups were compared, one-way analysis of variance (ANOVA) with Bonferroni post-hoc test was used. All statistical analyses display individual values for each biological replicate, mean value, and standard error of the mean (SEM). Statistical significance was set at $P < 0.05$.

REFERENCES AND NOTES

1. K. Alves de Lima, J. Rustenhoven, J. Kipnis, Meningeal Immunity and Its Function in Maintenance of the Central Nervous System in Health and Disease. *Annu. Rev. Immunol.* **38**, 597–620 (2020). doi: [10.1146/annurev-immunol-102319-103410](https://doi.org/10.1146/annurev-immunol-102319-103410); pmid: [32340575](https://pubmed.ncbi.nlm.nih.gov/32340575/)
2. B. Engelhardt, P. Vajkoczy, R. O. Weller, The movers and shapers in immune privilege of the CNS. *Nat. Immunol.* **18**, 123–131 (2017). doi: [10.1038/ni.3666](https://doi.org/10.1038/ni.3666); pmid: [28092374](https://pubmed.ncbi.nlm.nih.gov/28092374/)
3. R. Rua, D. B. McGavern, Advances in Meningeal Immunity. *Trends Mol. Med.* **24**, 542–559 (2018). doi: [10.1016/j.molmed.2018.04.003](https://doi.org/10.1016/j.molmed.2018.04.003); pmid: [29731353](https://pubmed.ncbi.nlm.nih.gov/29731353/)
4. F. Herisson *et al.*, Direct vascular channels connect skull bone marrow and the brain surface enabling myeloid cell migration. *Nat. Neurosci.* **21**, 1209–1217 (2018). doi: [10.1038/s41593-018-0213-2](https://doi.org/10.1038/s41593-018-0213-2); pmid: [30150661](https://pubmed.ncbi.nlm.nih.gov/30150661/)
5. R. Cai *et al.*, Panoptic imaging of transparent mice reveals whole-body neuronal projections and skull-meninges connections. *Nat. Neurosci.* **22**, 317–327 (2019). doi: [10.1038/s41593-018-0301-3](https://doi.org/10.1038/s41593-018-0301-3); pmid: [30598527](https://pubmed.ncbi.nlm.nih.gov/30598527/)
6. H. Yao *et al.*, Leukaemia hijacks a neural mechanism to invade the central nervous system. *Nature* **560**, 55–60 (2018). doi: [10.1038/s41586-018-0342-5](https://doi.org/10.1038/s41586-018-0342-5); pmid: [30022166](https://pubmed.ncbi.nlm.nih.gov/30022166/)
7. H. Keren-Shaul *et al.*, A Unique Microglia Type Associated with Restricting Development of Alzheimer's Disease. *Cell* **169**, 1276–1290.e17 (2017). doi: [10.1016/j.cell.2017.05.018](https://doi.org/10.1016/j.cell.2017.05.018); pmid: [28602351](https://pubmed.ncbi.nlm.nih.gov/28602351/)
8. S. Mundt *et al.*, Conventional DCs sample and present myelin antigens in the healthy CNS and allow parenchymal T cell entry to initiate neuroinflammation. *Sci. Immunol.* **4**, eaau8380 (2019). doi: [10.1126/sciimmunol.aau8380](https://doi.org/10.1126/sciimmunol.aau8380); pmid: [30679199](https://pubmed.ncbi.nlm.nih.gov/30679199/)
9. R. C. Rickert, J. Roes, K. Rajewsky, B lymphocyte-specific, Cre-mediated mutagenesis in mice. *Nucleic Acids Res.* **25**, 1317–1318 (1997). doi: [10.1093/nar/25.6.1317](https://doi.org/10.1093/nar/25.6.1317); pmid: [9092650](https://pubmed.ncbi.nlm.nih.gov/9092650/)
10. A. Louveau *et al.*, CNS lymphatic drainage and neuroinflammation are regulated by meningeal lymphatic vasculature. *Nat. Neurosci.* **21**, 1380–1391 (2018). doi: [10.1038/s41593-018-0227-9](https://doi.org/10.1038/s41593-018-0227-9); pmid: [30224810](https://pubmed.ncbi.nlm.nih.gov/30224810/)
11. J. H. Ahn *et al.*, Meningeal lymphatic vessels at the skull base drain cerebrospinal fluid. *Nature* **572**, 62–66 (2019). doi: [10.1038/s41586-019-1419-5](https://doi.org/10.1038/s41586-019-1419-5); pmid: [31341278](https://pubmed.ncbi.nlm.nih.gov/31341278/)
12. J. W. Tung, M. D. Mrazek, Y. Yang, L. A. Herzenberg, L. A. Herzenberg, Phenotypically distinct B cell development pathways map to the three B cell lineages in the mouse. *Proc. Natl. Acad. Sci. U.S.A.* **103**, 6293–6298 (2006). doi: [10.1073/pnas.0511305103](https://doi.org/10.1073/pnas.0511305103); pmid: [16606838](https://pubmed.ncbi.nlm.nih.gov/16606838/)
13. R. R. Hardy, C. E. Carmack, S. A. Shinton, J. D. Kemp, K. Hayakawa, Resolution and characterization of pro-B and

- pre-pro-B cell stages in normal mouse bone marrow. *J. Exp. Med.* **173**, 1213–1225 (1991). doi: [10.1084/jem.173.5.1213](https://doi.org/10.1084/jem.173.5.1213); pmid: [1827140](https://pubmed.ncbi.nlm.nih.gov/1827140/)
14. N. Kuwata, H. Igarashi, T. Ohmura, S. Aizawa, N. Sakaguchi, Cutting edge: Absence of expression of RAG1 in peritoneal B-1 cells detected by knocking into RAG1 locus with green fluorescent protein gene. *J. Immunol.* **163**, 6355–6359 (1999). pmid: [10586023](https://pubmed.ncbi.nlm.nih.gov/10586023/)
15. J. DeSisto *et al.*, Single-Cell Transcriptomic Analyses of the Developing Meninges Reveal Meningeal Fibroblast Diversity and Function. *Dev. Cell* **54**, 43–59.e4 (2020). doi: [10.1016/j.devcel.2020.06.009](https://doi.org/10.1016/j.devcel.2020.06.009); pmid: [32634398](https://pubmed.ncbi.nlm.nih.gov/32634398/)
16. F. Schena *et al.*, Dependence of immunoglobulin class switch recombination in B cells on vesicular release of ATP and CD73 ectonucleotidase activity. *Cell Rep.* **3**, 1824–1831 (2013). doi: [10.1016/j.celrep.2013.05.022](https://doi.org/10.1016/j.celrep.2013.05.022); pmid: [23770243](https://pubmed.ncbi.nlm.nih.gov/23770243/)
17. J. Rustenhoven *et al.*, Functional characterization of the dural sinuses as a neuroimmune interface. *Cell* **184**, 1000–1016.e27 (2021). doi: [10.1016/j.cell.2020.12.040](https://doi.org/10.1016/j.cell.2020.12.040); pmid: [33508229](https://pubmed.ncbi.nlm.nih.gov/33508229/)
18. N. Almanzar *et al.*, Tabula Muris Consortium, A single-cell transcriptomic atlas characterizes ageing tissues in the mouse. *Nature* **583**, 590–595 (2020). doi: [10.1038/s41586-020-2496-1](https://doi.org/10.1038/s41586-020-2496-1); pmid: [32669714](https://pubmed.ncbi.nlm.nih.gov/32669714/)
19. D. A. Mogilenko *et al.*, Comprehensive Profiling of an Aging Immune System Reveals Clonal GZMK⁺ CD8⁺ T Cells as Conserved Hallmark of Inflammation. *Immunity* **54**, 99–115.e12 (2021). doi: [10.1016/j.immuni.2020.11.005](https://doi.org/10.1016/j.immuni.2020.11.005); pmid: [33271118](https://pubmed.ncbi.nlm.nih.gov/33271118/)
20. Z. Fitzpatrick *et al.*, Gut-educated IgA plasma cells defend the meningeal venous sinuses. *Nature* **587**, 472–476 (2020). doi: [10.1038/s41586-020-2886-4](https://doi.org/10.1038/s41586-020-2886-4); pmid: [33149302](https://pubmed.ncbi.nlm.nih.gov/33149302/)
21. T. Goldmann *et al.*, Origin, fate and dynamics of macrophages at central nervous system interfaces. *Nat. Immunol.* **17**, 797–805 (2016). doi: [10.1038/ni.3423](https://doi.org/10.1038/ni.3423); pmid: [27135602](https://pubmed.ncbi.nlm.nih.gov/27135602/)
22. M. J. C. Jordão *et al.*, Single-cell profiling identifies myeloid cell subsets with distinct fates during neuroinflammation. *Science* **363**, eaat7554 (2019). doi: [10.1126/science.aat7554](https://doi.org/10.1126/science.aat7554); pmid: [30679343](https://pubmed.ncbi.nlm.nih.gov/30679343/)
23. H. Van Hove *et al.*, A single-cell atlas of mouse brain macrophages reveals unique transcriptional identities shaped by ontogeny and tissue environment. *Nat. Neurosci.* **22**, 1021–1035 (2019). doi: [10.1038/s41593-019-0393-4](https://doi.org/10.1038/s41593-019-0393-4); pmid: [31061494](https://pubmed.ncbi.nlm.nih.gov/31061494/)
24. D. Mrdjen *et al.*, High-Dimensional Single-Cell Mapping of Central Nervous System Immune Cells Reveals Distinct Myeloid Subsets in Health, Aging, and Disease. *Immunity* **48**, 380–395.e6 (2018). doi: [10.1016/j.immuni.2018.01.011](https://doi.org/10.1016/j.immuni.2018.01.011); pmid: [29426702](https://pubmed.ncbi.nlm.nih.gov/29426702/)
25. C. Fistonik *et al.*, Cell circuits between B cell progenitors and IL-7⁺ mesenchymal progenitor cells control B cell development. *J. Exp. Med.* **215**, 2586–2599 (2018). doi: [10.1084/jem.20180778](https://doi.org/10.1084/jem.20180778); pmid: [30158115](https://pubmed.ncbi.nlm.nih.gov/30158115/)
26. Y. Nie *et al.*, The role of CXCR4 in maintaining peripheral B cell compartments and humoral immunity. *J. Exp. Med.* **200**, 1145–1156 (2004). doi: [10.1084/jem.20041185](https://doi.org/10.1084/jem.20041185); pmid: [15520246](https://pubmed.ncbi.nlm.nih.gov/15520246/)
27. J. Zikherman, R. Parameswaran, A. Weiss, Endogenous antigen tunes the responsiveness of naive B cells but not T cells. *Nature* **489**, 160–164 (2012). doi: [10.1038/nature11311](https://doi.org/10.1038/nature11311); pmid: [22902503](https://pubmed.ncbi.nlm.nih.gov/22902503/)
28. T. Litzenburger *et al.*, B lymphocytes producing demyelinating autoantibodies: Development and function in gene-targeted transgenic mice. *J. Exp. Med.* **188**, 169–180 (1998). doi: [10.1084/jem.188.1.169](https://doi.org/10.1084/jem.188.1.169); pmid: [9653093](https://pubmed.ncbi.nlm.nih.gov/9653093/)
29. J. K. A. Cugurra *et al.*, Skull and vertebral bone marrow are myeloid reservoirs for the meninges and CNS parenchyma. *Science* **373**, XXX (–YYY) (2021).
30. M. P. Cancro, Age-Associated B Cells. *Annu. Rev. Immunol.* **38**, 315–340 (2020). doi: [10.1146/annurev-immunol-092419-031130](https://doi.org/10.1146/annurev-immunol-092419-031130); pmid: [31986068](https://pubmed.ncbi.nlm.nih.gov/31986068/)
31. A. V. Rubtsov *et al.*, Toll-like receptor 7 (TLR7)-driven accumulation of a novel CD11c⁺ B-cell population is important for the development of autoimmunity. *Blood* **118**, 1305–1315 (2011). doi: [10.1182/blood-2011-01-331462](https://doi.org/10.1182/blood-2011-01-331462); pmid: [21543762](https://pubmed.ncbi.nlm.nih.gov/21543762/)
32. Y. Hao, P. O'Neill, M. S. Naradikian, J. L. Scholz, M. P. Cancro, A B-cell subset uniquely responsive to innate stimuli accumulates in aged mice. *Blood* **118**, 1294–1304 (2011). doi: [10.1182/blood-2011-01-330530](https://doi.org/10.1182/blood-2011-01-330530); pmid: [21562046](https://pubmed.ncbi.nlm.nih.gov/21562046/)
33. M. Manni *et al.*, Regulation of age-associated B cells by IRF5 in systemic autoimmunity. *Nat. Immunol.* **19**, 407–419 (2018). doi: [10.1038/s41590-018-0056-8](https://doi.org/10.1038/s41590-018-0056-8); pmid: [29483597](https://pubmed.ncbi.nlm.nih.gov/29483597/)
34. O. L. Rojas *et al.*, Circulating Intestinal IgA-Producing Cells Regulate Neuroinflammation via IL-10. *Cell* **176**, 610–624.e18 (2019). doi: [10.1016/j.cell.2018.11.035](https://doi.org/10.1016/j.cell.2018.11.035); pmid: [30612739](https://pubmed.ncbi.nlm.nih.gov/30612739/)

35. S. L. Hauser *et al.*, B-cell depletion with rituximab in relapsing-remitting multiple sclerosis. *N. Engl. J. Med.* **358**, 676–688 (2008). doi: [10.1056/NEJMoa0706383](https://doi.org/10.1056/NEJMoa0706383); pmid: [18272891](https://pubmed.ncbi.nlm.nih.gov/18272891/)
36. S. L. Hauser *et al.*, Ofatumumab versus Teriflunomide in Multiple Sclerosis. *N. Engl. J. Med.* **383**, 546–557 (2020). doi: [10.1056/NEJMoa1917246](https://doi.org/10.1056/NEJMoa1917246); pmid: [32757523](https://pubmed.ncbi.nlm.nih.gov/32757523/)
37. Y. Wang *et al.*, TREM2-mediated early microglial response limits diffusion and toxicity of amyloid plaques. *J. Exp. Med.* **213**, 667–675 (2016). doi: [10.1084/jem.20151948](https://doi.org/10.1084/jem.20151948); pmid: [27091843](https://pubmed.ncbi.nlm.nih.gov/27091843/)
38. B. D. Metscher, MicroCT for developmental biology: A versatile tool for high-contrast 3D imaging at histological resolutions. *Dev. Dyn.* **238**, 632–640 (2009). doi: [10.1002/dvdy.21857](https://doi.org/10.1002/dvdy.21857); pmid: [19235724](https://pubmed.ncbi.nlm.nih.gov/19235724/)
39. T. Stuart *et al.*, Comprehensive integration of single-cell data. *Cell* **177**, 1888–1902.e21 (2019). doi: [10.1016/j.cell.2019.05.031](https://doi.org/10.1016/j.cell.2019.05.031); pmid: [31178118](https://pubmed.ncbi.nlm.nih.gov/31178118/)
40. C. Hafemeister, R. Satija, Normalization and variance stabilization of single-cell RNA-seq data using regularized negative binomial regression. *Genome Biol.* **20**, 296 (2019). doi: [10.1186/s13059-019-1874-1](https://doi.org/10.1186/s13059-019-1874-1); pmid: [31870423](https://pubmed.ncbi.nlm.nih.gov/31870423/)
41. G. Finak *et al.*, MAST: A flexible statistical framework for assessing transcriptional changes and characterizing heterogeneity in single-cell RNA sequencing data. *Genome Biol.* **16**, 278 (2015). doi: [10.1186/s13059-015-0844-5](https://doi.org/10.1186/s13059-015-0844-5); pmid: [26653891](https://pubmed.ncbi.nlm.nih.gov/26653891/)
42. T. Le, *et al.*, BBrowser: Making single-cell data easily accessible (2020). bioRxiv 2020.12.11.414136 [Preprint]. 11 December 2020. doi: [10.1101/2020.12.11.414136](https://doi.org/10.1101/2020.12.11.414136)
43. P. Angerer *et al.*, destiny: Diffusion maps for large-scale single-cell data in R. *Bioinformatics* **32**, 1241–1243 (2016). doi: [10.1093/bioinformatics/btv715](https://doi.org/10.1093/bioinformatics/btv715); pmid: [26668002](https://pubmed.ncbi.nlm.nih.gov/26668002/)
44. K. Street *et al.*, Slingshot: Cell lineage and pseudotime inference for single-cell transcriptomics. *BMC Genomics* **19**, 477 (2018). doi: [10.1186/s12864-018-4772-0](https://doi.org/10.1186/s12864-018-4772-0); pmid: [29914354](https://pubmed.ncbi.nlm.nih.gov/29914354/)
45. Y. Zhou *et al.*, Metascape provides a biologist-oriented resource for the analysis of systems-level datasets. *Nat. Commun.* **10**, 1523 (2019). doi: [10.1038/s41467-019-09234-6](https://doi.org/10.1038/s41467-019-09234-6); pmid: [30944313](https://pubmed.ncbi.nlm.nih.gov/30944313/)
46. R. Browaeys, W. Saelens, Y. Saeys, NicheNet: Modeling intercellular communication by linking ligands to target genes. *Nat. Methods* **17**, 159–162 (2020). doi: [10.1038/s41592-019-0667-5](https://doi.org/10.1038/s41592-019-0667-5); pmid: [31819264](https://pubmed.ncbi.nlm.nih.gov/31819264/)
47. N. T. Gupta *et al.*, Change-O: A toolkit for analyzing large-scale B cell immunoglobulin repertoire sequencing data. *Bioinformatics* **31**, 3356–3358 (2015). doi: [10.1093/bioinformatics/btv359](https://doi.org/10.1093/bioinformatics/btv359); pmid: [26069265](https://pubmed.ncbi.nlm.nih.gov/26069265/)
48. J. A. Vander Heiden *et al.*, pRESTO: A toolkit for processing high-throughput sequencing raw reads of lymphocyte receptor repertoires. *Bioinformatics* **30**, 1930–1932 (2014). doi: [10.1093/bioinformatics/btu138](https://doi.org/10.1093/bioinformatics/btu138); pmid: [24618469](https://pubmed.ncbi.nlm.nih.gov/24618469/)
49. W. B. Alsoussi *et al.*, A Potently Neutralizing Antibody Protects Mice against SARS-CoV-2 Infection. *J. Immunol.* **205**, 915–922 (2020). doi: [10.4049/jimmunol.2000583](https://doi.org/10.4049/jimmunol.2000583); pmid: [32591393](https://pubmed.ncbi.nlm.nih.gov/32591393/)
50. N. T. Gupta *et al.*, Hierarchical Clustering Can Identify B Cell Clones with High Confidence in Ig Repertoire Sequencing Data. *J. Immunol.* **198**, 2489–2499 (2017). doi: [10.4049/jimmunol.1601850](https://doi.org/10.4049/jimmunol.1601850); pmid: [28179494](https://pubmed.ncbi.nlm.nih.gov/28179494/)
51. J. Q. Zhou, S. H. Kleinstein, Cutting Edge: Ig H Chains Are Sufficient to Determine Most B Cell Clonal Relationships. *J. Immunol.* **203**, 1687–1692 (2019). doi: [10.4049/jimmunol.1900666](https://doi.org/10.4049/jimmunol.1900666); pmid: [31484734](https://pubmed.ncbi.nlm.nih.gov/31484734/)

ACKNOWLEDGMENTS

We thank E. Lantelme for her excellent management of the flow cytometry core facility at the department of Pathology and Immunology (Washington University in St. Louis). We thank D. Bender and R. Lin from the Bursky Center for Human Immunology and Immunotherapy Programs (CHiIPs) for their invaluable support of sample preparation for CyTOF analysis and acquisition of CyTOF data. We thank B. Saunders, B. Zinselmeyer, and G. Randolph for their assistance with two-photon in vivo imaging. We thank Y. Chen and D. Holtzman for providing the anti-ApoE antibody. We also thank L. Adamo for providing CD19-Tomato mice for preliminary experiments, P. Allen for providing *Nur7^{GFP}* mice, A. Archambault for providing the *IGH^{MOG}* mice, N. Sakaguchi for providing *Rag1^{GFP}* mice, and K. Ayasoufi for

helping with the perfusion and shipment of *Rag1^{GFP}* samples. Lastly, we thank R. Pelanda, J. Andersson, F. Melchers, A. Pernis, P. Kendall, and A. Ellebedy for their critical comments and helpful suggestions during the preparation of this manuscript.

Funding: This research was supported in part by NIH RF1 AG051485, NIH RF1 AG059082 (M. Colonna), NIH R01AI104739 (S.H.K.), NIH F30 DK127540-01, NIH T32 DK 77653-28 (V.P.), the Gruber Foundation (M.W.), NIH K99 DK118110 (J.K.B.), and FA-2020-01-IBD-1 fellowship from the Lawrence C. Pakula, MD IBD Education and Innovation Fund (R.S.C.). **Author contributions:** S.B, W.W, V.P: conceptualization, data curation, formal analysis, methodology, investigation, software, validation, visualization, and writing the original draft. M.W., I.S.: formal analysis, methodology, and software. Z.J.G, J.K.B., N.J., R.S.C., A.S., D.A.M.: formal analysis and methodology. W.L.B., P.B., J.A.J.F., L.G.S., C.C.F., I.S., J.K., V.S., G.W., S.G.: methodology and resources. M.C., M.N.A., S.H.K.: supervision. M.Colonna: funding acquisition, supervision, project administration, manuscript review, and editing. **Competing interests:** S.H.K. receives consulting fees from Northrop Grumman. All other authors declare no conflict of interest. **Data and materials availability:** scRNA-seq and scBCR-seq data available from NCBI GEO with accession number GSE174836. All other data and materials are available in the paper and supplementary materials.

SUPPLEMENTARY MATERIALS

science.sciencemag.org/content/373/6553/eabf9277/suppl/DC1
Materials and Methods
Figs. S1 to S16
Tables S1 to S4
MDAR Reproducibility Checklist
Movies S1 and S2

[View/request a protocol for this paper from Bio-protocol.](#)

29 November 2020; resubmitted 1 April 2021
Accepted 24 May 2021
Published online 3 June 2021
[10.1126/science.abf9277](https://doi.org/10.1126/science.abf9277)

Heterogeneity of meningeal B cells reveals a lymphopoietic niche at the CNS borders

Simone BrioschiWei-Le WangVincent PengMeng WangIrina ShchukinaZev J. GreenbergJennifer K. BandoNatalia JaegerRafael S. CzepielewskiAmanda SwainDenis A. MogilenkoWandy L. BeattyPeter BayguinovJames A. J. FitzpatrickLaura G. SchuettpeizCatrina C. FronickIgor SmirnovJonathan KipnisVirginia S. ShapiroGregory F. WuSusan GilfillanMarina CellaMaxim N. ArtyomovSteven H. KleinsteinMarco Colonna

Science, 373 (6553), eabf9277. • DOI: 10.1126/science.abf9277

Getting around the blood–brain barrier

The meninges comprise three membranes that surround and protect the central nervous system (CNS). Recent studies have noted the existence of myeloid cells resident there, but little is known about their ontogeny and function, and whether other meningeal immune cell populations have important roles remains unclear (see the Perspective by Nguyen and Kubes). Cugurra *et al.* found in mice that a large proportion of continuously replenished myeloid cells in the dura mater are not blood derived, but rather transit from cranial bone marrow through specialized channels. In models of CNS injury and neuroinflammation, the authors demonstrated that these myeloid cells have an immunoregulatory phenotype compared with their more inflammatory blood-derived counterparts. Similarly, Brioschi *et al.* show that the meninges host B cells that are also derived from skull bone marrow, mature locally, and likely acquire a tolerogenic phenotype. They further found that the brains of aging mice are infiltrated by a second population of age-associated B cells, which come from the periphery and may differentiate into autoantibody-secreting plasma cells after encountering CNS antigens. Together, these two studies may inform future treatment of neurological diseases.

Science, abf7844, abf9277, this issue p. eabf7844, p. eabf9277; see also abj8183, p. 396

View the article online

<https://www.science.org/doi/10.1126/science.abf9277>

Permissions

<https://www.science.org/help/reprints-and-permissions>

Use of this article is subject to the [Terms of service](#)

Science (ISSN 1095-9203) is published by the American Association for the Advancement of Science, 1200 New York Avenue NW, Washington, DC 20005. The title *Science* is a registered trademark of AAAS.

Copyright © 2021 The Authors, some rights reserved; exclusive licensee American Association for the Advancement of Science. No claim to original U.S. Government Works